Cite as: H. Yu *et al.*, *Science* 10.1126/science.abb4309 (2020).

HSP70 chaperones RNA-free TDP-43 into anisotropic intranuclear liquid spherical shells

Haiyang Yu[1]*, Shan Lu[1]†, Kelsey Gasior[2,3]†‡, Digvijay Singh[4], Sonia Vazquez-Sanchez[1], Olga Tapia[5,6], Divek Toprani[1], Melinda S. Beccari[1,7], John R. Yates III[8], Sandrine Da Cruz[1,9,10], Jay M. Newby[11], Miguel Lafarga[5,6,12], Amy S. Gladfelter[2,13], Elizabeth Villa[4], Don W. Cleveland[1,7]*

[1]Ludwig Institute for Cancer Research, University of California at San Diego, La Jolla, CA, USA. [2]University of North Carolina Chapel Hill, Department of Biology, Chapel Hill, NC, USA. [3]University of North Carolina Chapel Hill, Department of Mathematics, Chapel Hill, NC, USA. [4]Division of Biological Sciences, University of California, San Diego, San Diego, CA, USA. [5]"Centro de Investigación Biomedica en Red sobre Enfermedades Neurodegenerativas" (CIBERNED), Madrid, Spain. [6]"Instituto de Investigación Sanitaria Valdecilla" (IDIVAL), Santander, Spain. [7]Department of Cellular and Molecular Medicine, University of California at San Diego, La Jolla, CA, USA. [8]Departments of Molecular Medicine and Neurobiology, The Scripps Research Institute, La Jolla, CA, USA. [9]VIB-KU Leuven Center for Brain & Disease Research, Leuven, Belgium. [10]Department of Neurosciences, KU Leuven, Leuven, Belgium. [11]Department of Mathematical and Statistical Sciences, University of Alberta, Edmonton, Alberta, Canada T6G 2G1. [12]Department of Anatomy and Cell Biology, University of Cantabria, Santander, Spain. [13]Marine Biological Laboratory, Woods Hole, MA, USA.

***Corresponding author. Email: dcleveland@ucsd.edu (D.W.C.); haiyang-yu@ucsd.edu (H.Y.)**

†These authors contributed equally to this work.
‡Present address: Florida State University Department of Mathematics, 1017 Academic Way, Tallahassee, FL 32304, USA.

The RNA-binding protein TDP-43 forms intranuclear or cytoplasmic aggregates in age-related neurodegenerative diseases. Here we found that RNA-binding deficient TDP-43 (produced by neurodegeneration-causing mutations or post-translational acetylation in its RNA recognition motifs) drove TDP-43 de-mixing into intranuclear liquid spherical shells with liquid cores. We named these droplets anisosomes, whose shells exhibited birefringence, evidence of liquid crystal formation. Guided by mathematical modeling, we identified the major components of the liquid core to be HSP70 family chaperones, whose ATP-dependent activity maintained the liquidity of shells and cores. In vivo proteasome inhibition within neurons, to mimic aging-related reduction of proteasome activity, induced TDP-43-containing spherical shells. These structures converted into aggregates when ATP levels were reduced. Thus, acetylation, HSP70, and proteasome activities regulate TDP-43 phase separation and conversion into a gel/solid phase.

Mislocalization and aggregation of TDP-43 (TAR DNA-binding protein 43), a nuclear RNA-binding protein, is a pathological hallmark shared by several age-related neurodegenerative diseases. These include amyotrophic lateral sclerosis (ALS) (*1*), frontotemporal dementia (FTD) (*2*), Alzheimer's disease (AD) (*3*), and the recently defined AD-like variant named "LATE" (limbic predominant age-related TDP-43 encephalopathy) in the oldest individuals (*4*). TDP-43 functions in pre-mRNA maturation, including splicing (*5*). Nuclear aggregation of TDP-43 is also found in affected brain regions of FTD and AD patients (*6*–*9*), although it has often been overlooked in pathological analyses focused on phosphorylated TDP-43 aggregates found in the cytoplasm.

TDP-43 naturally de-mixes in the nucleus (*10*), but can be induced by multiple stresses to accumulate in the cytoplasm. Loss of nuclear TDP-43 causes cryptic splicing (*11*–*13*) and premature polyadenylation (*13*), dysregulating many important neuronal genes, including HSPA8 (*14*), HDAC6 (*15*), and stathmin-2 (*11*, *13*). The RNA-binding activity of TDP-43 is inhibited by post-translational acetylation on two lysine residues (K145 and K192) (*16*). Additionally, acetylated TDP-43 accumulates in cytoplasmic aggregates in the nervous systems of ALS patients (*16*).

A seminal discovery in the last decade is the recognition that proteins, nucleic acids, or a mixture of both can de-mix into two phases, a condensed de-mixed phase and a dilute aqueous phase, resembling oil droplets in vinegar, a phenomenon called liquid-liquid phase separation (LLPS) (*17*). The condensed phase can form membraneless organelles that have been proposed to promote biological functions (*18*). Discovery that P-granules are de-mixed compartments with liquid behavior brought widespread recognition to LLPS and its ability to mediate subcellular compartmentalization in a biological context (*19*). Phase separation has also been proposed for heterochromatin and RNA bodies (*17*, *19*, *20*).

LLPS potentially underlies the operational principle governing formation of important organelles and structures, such as centrosomes, nuclear pore complexes, and super enhancers (*21*–*23*). Beyond two-phase LLPS, a condensed phase can further de-mix into an additional internalized gel. This behavior has been observed for example in the nucleolus (*24*) or paraspeckles (*24*–*26*), in gel-like droplets adjacent to liquid

P-granules (*27*), in a gel-like core surrounded by a liquid shell (*28*), or in multiphase liquid droplets of an overexpressed TDP-43 in which its RNA-binding domains have been replaced with GFP (*29*) or simply removed (*30*). LLPS of proteins, especially RNA-binding proteins, is currently explained by multi-valent interactions of low complexity domains that are intrinsically disordered (*31*), with no ordered alignments within the condensed liquid phase.

Here we report an interesting LLPS phenomenon, intranuclear droplets with anisotropic liquid spherical shells and liquid cores, driven by RNA-binding compromised TDP-43 produced by its reversible post-translational acetylation, ALS-causing mutations, or proteasome inhibition. It produced close-to-perfect liquid spherical shells with a high TDP-43 concentration and an inner liquid spherical core enriched in HSP70 family chaperones, forming a "liquid-inside-a-liquid-inside-a-liquid." Because of its anisotropy and the differential ("uneven") distribution of TDP-43 within this unique membraneless compartment, we named it "anisosome," from Greek words "ánisos" and "soma," meaning "uneven body." Shells exhibited birefringence, validating them to be liquid crystals that form from protein within a living cell. In vivo proteasome inhibition, to mimic reduction in proteasome activity during aging (*32*, *33*), induced TDP-43-containing anisosomes to convert into aggregates after ATP reduction.

RNA-binding deficient TDP-43 de-mixes into liquid spherical shells in physiological conditions

TDP-43 contains an N-terminal self-association domain (*34*, *35*), a C-terminal LCD, and two conserved RNA recognition motifs (RRM1 and RRM2). Its RNA-binding capacity can be reduced by ALS or FTD-causing mutations (P112H, K181E or K263E) (*36*–*38*) or eliminated by post-translational acetylation of two lysine residues (K145 in RRM1 and K192 in RRM2) (*16*) or by replacing five phenylalanine residues in the two RRMs that interact with RNA (*39*) (Fig. 1A). Cell clones were generated in which full length, RNA-binding deficient TDP-43 variants (each fluorescently tagged with clover) could be induced to accumulate from 0.3- to 9-fold the initial physiological TDP-43 level (fig. S1, A to F). Wildtype TDP-43^{clover} formed nuclear droplets (Fig. 1B), as expected (*10*). In contrast, each of the RNA-binding deficient TDP-43 variants (including acetylation-mimicking mutant TDP-43^{K145Q,K192Q} in which glutamines replaced the two lysines that are acetylated in TDP-43 (*16*) and hereafter named TDP-43^{2KQ}), TDP-43^{5FL} (in which five phenylalanines were substituted to leucines (*39*)), or ALS/FTD causing mutations TDP-43^{P112H} (*36*), TDP-43^{K181E} (*37*) and TDP-43^{K263E} (*38*) formed close-to-perfectly spherical intranuclear droplets in which TDP-43 was enriched in an outer shell but depleted in the center (Fig. 1, B and C, and fig. S1B). This did not require overexpression—it was observed at RNA-binding deficient TDP-43 levels as low as 0.3 times the level of endogenous TDP-43 (Fig. 1D). De-mixing of TDP-43 into spherical shells with apparently hollow cores was observed over a broad range of accumulation of each RNA-binding compromised TDP-43 variant (e.g., for TDP-43^{2KQ} between 0.3 and 9 fold TDP-43's normal level (Fig. 1D and fig. S1, D to F)). The fraction of spherical shell-containing nuclei (Fig. 1E) and number of the spheres per nucleus depended on the variant (Fig. 1F), likely owing to the remaining level of RNA-affinity and the expression level (Fig. 1, B and D).

Fluorescence Recovery After Photobleaching (FRAP) was used to determine that RNA-binding deficient TDP-43 enriched in spherical shells freely exchanged with TDP-43 in the nucleoplasm (e.g., TDP-43$^{2KQ\text{-}clover}$ - a mimic of acetylated wildtype TDP-43 (*16*) - recovered after bleaching with a $t_{1/2}$ of 9 s - Fig. 1G). 3D live cell imaging of intranuclear nuclear droplets containing TDP-43$^{2KQ\text{-}clover}$ (unambiguously identified in Z projections to be enriched in spherical shells – fig. S1G and movie S1) revealed that these droplets frequently fused to form larger droplets (fig. S1H). Furthermore, direct comparison of fluorescence and differential interference contrast (DIC) imaging revealed that these liquid spherical shells could be directly observed in DIC images (Fig. 1H). Live cell DIC imaging (movie S2) detected abundant, rapid (within 10 s) fusion events in which the shells fused with each other, as did the cores, indicating that both shells and cores behave like liquids.

Deacetylase or proteasome inhibition drives wildtype TDP-43 to form spherical shells

Inhibition of deacetylases (with the pan deacetylase inhibitors trichostatin A (TSA) or vorinostat (a.k.a. SAHA)) in cells with fluorescently tagged TDP-43 (TDP-43$^{WT\text{-}clover}$) replacing endogenous TDP-43 was sufficient to drive it into spherical shells (fig. S1I). Similarly, increasing acetylation by expression of a known acetyltransferase [the core component of transcription initiation complex CEBP-binding protein (CBP) (*40*, *41*)] also drove TDP-43$^{WT\text{-}clover}$ into spherical droplets (fig. S1I), whose number increased markedly and morphology became spherical shells after addition of either deacetylase inhibitor.

Because RNA-binding deficient TDP-43 is quickly degraded by nuclear proteasomes (*42*), we reasoned that demixing of acetylated TDP-43 could be enhanced by inhibiting the proteasome. Indeed, while deacetylase inhibition alone caused only a small increase of TDP-43-containing droplets in neuron-like SHSY-5Y cells, both the numbers and diameters of these shells were enhanced by transient, partial inhibition of proteasome activity (by addition of the FDA-approved bortezomib (BTZ) for 4 hours) (Fig. 1I). Such demixing of wildtype TDP-43 did not require elevating its expression. Wildtype TDP-43 expressed from endogenous

alleles de-mixed into spherical shells upon deacetylase and proteasome inhibition in induced pluripotent stem cell (iPSC)-derived human motor neurons (Fig. 1J). Thus, TDP-43 naturally undergoes acetylation and deacetylation in these neurons.

Anisosomes – TDP-43 liquid spherical shells with liquid crystalline properties

Liquid crystals flow like a conventional liquid but contain non-randomly oriented molecules producing a birefringent, anisotropic liquid (*43*). Complete extinction microscopy with a pair of polarizers perpendicular to each other (Fig. 2, A and B), conditions in which image brightness correlates with the level of anisotropy (*44*), was used to determine that the shells (but not cores) of RNA-binding deficient TDP-43 droplets were the only non-membrane component visible, indicating anisotropic subdomains (Fig. 2C and movie S3). Live imaging provided further evidence of the liquid properties of the shells, with the positions of the ordered subdomains changing faster than our (180 ms) detection limit (Fig. 2C). As expected, lipid bilayers of all cellular membrane compartments, another biological liquid crystal (*45*), were also visible, while de-mixed nucleoli (*26*) were not distinguished from surrounding nucleoplasm (Fig. 2, D and E). Because of the uneven distribution of TDP-43 in these droplets, and their anisotropic property, we named these intranuclear TDP-43 droplets "anisosomes."

Anisotropy of ordered biomacromolecules changes or disappears as temperature increases (*46*, *47*) because increased entropy changes the interaction between the biomacromolecules that mediate the anisotropic alignment. Consequently, we performed live DIC imaging during temperature increase from 37° to 39°C (fig. S2, A to F, and movie S4). Anisosomes gradually transformed into uniform liquid droplets (fig. S2D) that fused and changed shape over time (fig. S2E). Uniform oval droplets reconverted into anisosomes as the temperature was reduced to 37°C (fig. S2F). Heat shock (20 min at 42°C) also transformed anisosomes into uniform droplets (fig. S2G).

RNA-binding deficient TDP-43 recruits wildtype TDP-43

Next, we tested if RNA-binding deficient TDP-43 recruited wildtype TDP-43 to phase separate into shells and cores of anisosomes. We started with a cell line (*10*) in which endogenously expressed TDP-43 was replaced with a fluorescently-tagged wildtype TDP-43 (hereafter TDP-43$^{WT\text{-}mRuby}$), with TDP-43 autoregulation (*5*, *48*) maintaining normal TDP-43 level (fig. S3, A and B). We then introduced RNA-binding deficient TDP-43 variants, which, as expected, de-mixed into anisosomes and recruited TDP-43$^{WT\text{-}mRuby}$ (fig. S3C). Over an 18-hour course, TDP-43$^{WT\text{-}mRuby}$ was recruited with RNA-binding deficient TDP-43$^{5FL\text{-}clover}$ into anisosomes (fig. S3, D and E). Use of FRAP to bleach either the RNA-binding deficient mutant TDP-43$^{5FL\text{-}clover}$ or TDP-43$^{WT\text{-}mRuby}$ within half of a nucleus revealed comparably rapid kinetics of recovery of red and green fluorescence within both shells and cores of individual bleached droplets, with corresponding fluorescence losses from unbleached droplets (fig. S3, F and G). Thus, RNA-binding deficient TDP-43 effectively recruits wildtype TDP-43 into the anisosomes.

TDP-43 anisosomes are densely packed membraneless compartments

Conventional transmission electron microscopy (TEM) revealed that despite the liquid character of anisosomal shells and cores, the liquid shells were easily visualized (with a standard OsO_4 staining protocol) following induction of RNA-binding deficient TDP-43^{2KQ}, but not TDP-43^{WT} (Fig. 3, A to C). Cross sections of TDP-43 anisosomes were close-to-perfect annuli of diameters between 0.5 and 2 μm (Fig. 3C and fig. S4). Distribution of TDP-43$^{2KQ\text{-}clover}$ molecules across the shells was determined using 70~80 nm ultrathin sections of fixed cells incubated with gold particle-labeled GFP antibody that also recognizes clover. Antibody-bound gold particles were highly enriched in the shell, slightly enriched in the core, and very sparse in the nucleoplasm (Fig. 3D and fig. S5). In contrast, TDP-43$^{WT\text{-}clover}$ formed droplets in which TDP-43 was uniformly distributed (Fig. 3D).

The average shell thickness was largely independent of the diameter of the anisosome (fig. S4, G to I). Some (~10%) anisosomal sections contained electron-lucent regions in the electron-dense shell, consistent with fusion events or a liquid phase exchanging between the inner droplet and the nucleoplasm (fig. S4G). Use of TEM confirmed the temperature-dependent conversion from anisosomes to uniform droplets. Transient incubation at elevated temperature (20 min at 39°C) partially disrupted the shell structure, producing more irregular shapes, while at 42°C the shell disappeared, yielding uniform droplets of lighter electron density than anisosomes and which were still distinguished from the nucleoplasm (Fig. 3, E and F).

The structure of anisosomes under physiological conditions in cells was determined with cryo-electron tomography (CryoET) (Fig. 3G). After creating thin lamellae (with cryo-FIB milling) (fig. S6), tomographic reconstructions revealed that anisosomes had a well-defined annular ring of 320 nm ± 20 nm thickness, consisting of meshwork-like densities similar to the meshwork reported in tomographic images of in vitro reconstituted phase-separated compartments (*49*). Molecular density in the anisosomal core appeared lower than in adjacent nucleoplasm (Fig. 3H). The tomograms revealed that anisosomal structure was consistent with a liquid center surrounded by a porous, meshwork-like rim through which some molecules can shuttle.

Reduced proteasome activity drives anisosome formation within neurons in vivo

Recognizing that proteosome activity in the mammalian nervous system declines with age (*33*), we used peripheral injection of the proteasome inhibitor BTZ to reduce its activity within rat dorsal root ganglion neurons (DRG). This produced easily observable intranuclear annular structures (0.2 – 1 μm in diameter), whose shells were enriched in endogenous, wildtype TDP-43 (as determined using immunogold electron microscopy - Fig. 4, A to C).

While nuclear aggregates, but not anisosomes, of TDP-43 have been repeatedly reported in postmortem samples of FTD and AD patients (*8*, *9*), we tested if TDP-43-containing anisosomes would be maintained following the delays inherent in sample collection for human postmortem analyses. Following peripheral injection of a proteasome inhibitor, DRGs were collected freshly or after a 2-hour postmortem interval sufficient for ATP depletion (Fig. 4D). Electron microscopic analyses of the DRGs revealed that the freshly perfused samples preserved anisosomal structure (Fig. 4E), while as short as a 2-hour postmortem delay (during which rigor mortis initiated from depleted ATP levels) yielded complete loss of anisosomes and their replacement with nuclear aggregates (Fig. 4F).

TDP-43 anisosomes are a selective barrier to some intranuclear components

Examination of anisosomal shells from RNA-binding deficient TDP-43 revealed the exclusion of several intranuclear components, including chromatin (marked by histone H2B - Fig. 5A), behavior similar to LLPS of artificial nuclear proteins and consistent with exclusion mediated by surface tension (*50*). Some RNA-binding proteins were also excluded, including FUS (mutations in which cause ALS) and iavNP, an RNA-binding protein encoded by the human influenza A virus (Fig. 5B). Other RNA-binding proteins (hnRNPA2B1, hnRNPH1 and hnRNPK), however, freely diffused into both the shell and core (Fig. 5C). Nuclear-targeted GFP (*51*) also diffused freely across the shell (Fig. 5B). Recognizing that anisosomes contained both RNA-binding deficient and wildtype TDP-43, as well as other RNA-binding proteins, we then determined RNA content by using CLICK-chemistry to fluorescently label RNA after incorporation of 5-ethynyl uridine (5-eU) (Fig. 5D). Imaging of individual anisosomes and surrounding nucleoplasm revealed that RNA was depleted from shells and cores relative to nucleoplasm (Fig. 5, E and F).

Remarkably, intranuclear anisosomes remained intact after exposure to the cytoplasm during mitosis (Fig. 5G) and were then excluded from newly forming post-mitotic nuclei in earliest interphase (Fig. 5, G and H). RNA-binding deficient TDP-43^{2KQ} was likely re-imported into daughter nuclei and reassembled into anisosomes within 2 hours after mitotic exit, because the size of cytoplasmic droplets decreased quickly within 10 min (see droplets #1-7, Fig. 5H). Anisosomes also formed in micronuclei produced by chromosome mis-segregation and there was an increase of total number of anisosomes within the two daughter nuclei, as expected from TDP-43 re-importation through nuclear pores (Fig. 5H).

Oligomerization and prion-like domains of TDP-43 are required for anisosome formation

To identify the interactions that maintain anisosomal structure, we first determined that forcing RNA-binding deficient TDP-43 to accumulate in the cytoplasm (by mutation of the nuclear localization sequence) largely eliminated anisosomes (fig. S7, A and B). TDP-43 possesses an N-terminal self-interaction domain (NTD) (*34*) that mediates its oligomerization (fig. S7, C and D) through three intermolecular salt bridges (*34*, *35*). Disrupting self-interaction [by converting serine 48 in one bridge to a phosphorylation mimicking residue (glutamic acid) or by mutating glycine 53 to aspartic acid that is part of forming a second bridge (fig. S7, E and F)] completely disrupted anisosomal formation of TDP-43. The NTD alone did not form intranuclear droplets or anisosomes. However, it was sufficient to drive intranuclear phase separation into droplets, but not anisosomes, when linked to LCD domains from FUS or EWS (fig. S7, G and H), other RNA-binding proteins known to be able to phase separate (*52*).

TDP-43 is the only hnRNP that contains a folded, self-interacting N-terminal domain, which is likely to enable its phase separation into anisotropic droplets. Indeed, while many efforts have focused on how phase separation is mediated by LCDs, single amino acid changes in its amino terminus are sufficient to block anisosomes assembled from RNA-binding deficient TDP-43 (fig. S7, E and F), consistent with self-interaction of the N-terminal domain mediated by salt bridges formed by residues Gly53 and Ser48 of one unit with Glu17 of the neighboring unit (*34*). A disease-causing mutation (G335D) that partially disrupts the helices formed by the conserved region in the LCD of TDP-43 (*53*) did not affect anisosomal structure (fig. S7I). Similarly, anisosomal structure was not affected by a corresponding variant (G335A) that decreased the dynamics of de-mixed LCD droplets in vitro (fig. S7J) (*53*).

Modeling predicts a low affinity TDP-43 partner in the anisosomal core

To identify mechanisms that can drive anisosomal formation, we created a mathematical model of an RNA-binding deficient TDP-43 in the presence of RNA (as it would be in a cell). Because the majority of TDP-43 molecules form stable dimers or even oligomers in vitro (*35*, *54*) and perhaps in vivo (*34*, *55*) and because nuclei have a high RNA concentration (Fig. 5F and fig. S8), we modeled a de-mixing system that included

RNA and monomers and dimers of the acetylation-mimicking TDP-43^{2KQ}, neither of which have affinity for the RNA (Fig. 6A). We employed a Cahn Hilliard diffuse interface model coupled with a Flory Huggins free energy scheme that employs the parameter χ to describe the energetic favorability of different components mixing in the system. Each pair of solute species had a parameter χ representing their energy cost of mixing. Higher values of χ represented a larger energy cost, favoring de-mixing. In this model, two TDP-43^{2KQ} monomers (P) came together to form the TDP-43 dimer (P_2). We further assumed that once formed, it was energetically unfavorable for the dimer (P_2) to mix with both the nucleoplasm and the RNA. Conversely, RNA was diffusely distributed throughout nucleoplasm. With this modeling structure, TDP-43^{2KQ} monomers formed dimers (P_2) which then rapidly de-mixed from the RNA-containing nucleoplasm forming only uniform droplets, not spherical shells (fig. S8D).

Because a simple mixture of acetylated TDP-43 and RNA failed to form anisosomes in our initial model, we extended it to include a hypothetical entity, Y, representing one or more proteins that possessed both self-interaction and propensity to de-mix with TDP-43^{2KQ} dimer. This approach built upon prior modeling work in which two components from a surrounding solution de-mixed into the same droplet, with one occupying the spherical core and the other forming a shell between the droplet core and the diffuse phase (*56*). Binding interaction energies and initial conditions were sampled to determine conditions that favored annuli formation. In particular, annuli formation was sensitive to the initial ratio between Y and the TDP43 monomer, as well as the ratio of the binding interaction kinetics for TDP43 dimer formation. However, there was a robust range of parameter values that allowed for this phenomenon to occur. Upon introducing this hypothetical Y protein into the model, shell de-mixing was induced, but only when TDP-43 dimer bound Y with an intermediate affinity (Fig. 6B and fig. S9).

Furthermore, because RNA was reduced inside the TDP-43 anisosomes (Fig. 5D), we also hypothesized that it was energetically unfavorable for Y to mix with the diffuse RNA. Introduction of Y into a mixture of TDP-43^{2KQ} and RNA successfully modeled de-mixing of TDP-43 into anisosome-like structures, with Y forming the core (Fig. 6B) and a predicted volume fraction of TDP-43 in the shell about two times that of the inner droplet (Fig. 6C). The model closely predicted the actual 2.3-2.9 fold experimentally measured ratio of TDP-43 in anisosomal shells and cores formed with TDP-43$^{2KQ\text{-clover}}$, as determined by fluorescence intensity from optical slices (Fig. 6, D to F) or immunogold electron microscopy (Fig. 6, G and H).

HSP70 family chaperones enrich in the liquid core of TDP-43 anisosomes

Because introduction of the unknown Y component allowed anisosome formation in our model, we used a proteomic approach to determine the identity(ies) of such components in the liquid cores of TDP-43 anisosomes. A combination of differential isotope labeling of cells with or without TDP-43 anisosomes was coupled with proximity labeling (with biotin) of proteins close to peroxidase tagged TDP-43 (fig. S10A), followed by immunoprecipitation and quantitative mass spectrometry (Fig. 7A). When stably expressed, TDP-43$^{mRuby2\text{-}APEX}$, a wildtype TDP-43 fused to red fluorescent protein (mRuby2) and peroxidase (APEX2) tags, accumulated intranuclearly with a proportion de-mixed into droplets (fig. S10B). Induction TDP-43$^{2KQ\text{-clover}}$ yielded co-de-mixing of the RNA-binding competent and incompetent TDP-43's into abundant anisosomes (fig. S10B).

Cells were isotope-labeled in the absence or presence of anisosomes and briefly exposed to H_2O_2 to enable APEX2 to label proximal proteins with biotin. Quantitative mass spectrometry revealed that the only proteins enriched at least 6-fold in TDP-43 anisosomes were the five members of the HSP70 family of ATP-dependent protein folding chaperones (HSPA1A, HSPA1L, HSPA5, HSPA6, and HSPA8), with each enriched between 6- and 16-fold (Fig. 7B). Indirect immunofluorescence could not be used to determine content of the cores because conventional fixation produces a barrier of crosslinked shell proteins that prevents antibody penetration to the core (fig. S11). Correspondingly, expression of mRuby2 tagged HSPA1A, HSPA1L, HSPA6 or HSPA8 was used to validate that each of these HSP70 family members was indeed enriched in the anisosomal cores (Fig. 7C).

ATP-dependent HSP70 chaperone activity maintains the anisosomal structure

Our mathematical modeling also predicted that anisosomal shells convert into uniformly phase separated droplets when the affinity between "Y" (HSP70) and TDP-43^{2KQ} is increased (fig. S12). We found that shells enriched in TDP-43 rapidly (and reversibly) merged with their liquid cores (fig. S2) when the HSP70 association with TDP-43 was enhanced by mild temperature increase (*57*). Each HSP70 family member requires ATP hydrolysis to fulfill its protein-folding chaperone function (*58*). After addition of an HSP70 inhibitor thought to block ATP hydrolysis by all family members (*59*) and to lock the chaperone onto a client protein (*58*), TDP-43^{2KQ} anisosomes converted within 10 min into small droplets of uniformly distributed TDP-43^{2KQ} and HSP70. In an additional 30-60 min, these droplets fused into a single large particle, whose formation was reversible, with anisosomes reforming within 6 min after removal of the HSP70 inhibitor (Fig. 8, A and D). HSP70 molecules in the liquid anisosomal cores were

highly dynamic, quickly recovering ($t_{1/2}$ = 3 s) after photobleaching (Fig. 8, C and D). After HSP70 inhibition, however, TDP-43$^{2KQ\text{-}clover}$ anisosomes converted into an intranuclear gel (with little recovery after photobleaching), while HSP70 in the particles retained liquid character, albeit with much slower ($t_{1/2}$ = 50 s) recovery after photobleaching. Importantly, transient depletion of ATP by blocking mitochondrial ATP synthesis and glucose starvation also caused anisosomes to collapse (fig. S13). Intracellular HSP70 interaction with TDP-43 was determined to be mediated primarily through its RRMs, with enhanced interaction with RNA-binding deficient TDP-43 (fig. S14). HSP70 did not form intranuclear membraneless condensates by itself (Fig. 7C) or in the absence of TDP-43 (fig. S15). Thus, we found no evidence of pre-existing liquid cores around which RNA-binding deficient TDP-43 condensed to form anisosomes.

Cytoplasmic TDP-43 aggregation has been observed in many age-related neurodegenerative diseases (*1*–*4*). The known reduction in nuclear/cytoplasmic transport during aging of the mammalian nervous system (*10*, *60*) would facilitate an age-dependent increase in cytoplasmic TDP-43. Recognizing this, and that HSP70 accumulates to a high level in the cytoplasm (Fig. 7C), we tested how reducing HSP70 chaperone activity affected cytoplasmic TDP-43 behavior following removal of its NLS to mimic age-dependent reduction in TDP-43 nuclear import (Fig. 8E). Within 1 hour after addition of the HSP70 inhibitor, cytoplasmic RNA-binding deficient TDP-43 converted from diffusely localized, soluble TDP-43 into round cytoplasmic droplets whose number and diameter increased with time (Fig. 8F). Furthermore, photobleaching revealed that initially liquid droplets converted into gel/solids, as indicated by slow, very partial fluorescence recovery after photobleaching (Fig. 8G).

Discussion

Here we report that ALS-causing mutations, acetylation-mimicking mutations, or increased acetylation of wildtype TDP-43–each of which reduces its RNA-binding–drove phase separation with RNA-binding competent TDP-43 into droplets comprised of an anisotropic, liquid spherical shell enriched in TDP-43 and a liquid core comprised of HSP70 family chaperones (as well as TDP-43), structures that we termed TDP-43 anisosomes. Liquidity of both shells and cores was dependent on continuing ATPase-dependent chaperone activity. Unlike previously identified intracellular liquid droplets, including the nucleolus (*24*), anisosomal cores were centrally aligned so as to produce symmetrical liquid shells. Cryo-electron tomography, traditional EM, and fluorescence microscopy of TDP-43 intranuclear anisosomes revealed the exclusion of chromatin and some RNA-binding proteins, while other RNA-binding proteins freely exchanged, as demonstrated with photobleaching. TDP-43 anisosomes exhibited birefringence, evidence that an anisotropic liquid could be formed intracellularly by protein phase separation in complex nucleoplasm. While acetylation of histones H1 and H3 has recently been reported to abolish liquid-liquid phase separation of chromatin (*61*), acetylation of TDP-43 did the opposite: it promoted phase separation. Recognizing that protein acetyltransferases are enriched in transcription initiation complexes (*40*), phase separation of TDP-43 near sites of transcription could form a barrier to include some but exclude other RNA-binding proteins and provide a means to facilitate pre-mRNA maturation.

Our modeling strongly supported an essential role for the HSP70 family of chaperones in anisosome formation–continuing chaperone activity was required for generation and maintenance of the liquidity of the shells and cores. Indeed, depletion of ATP induced anisosome collapse and conversion into aggregates of TDP-43 in cultured cells and in neurons of the murine nervous system following post-mortem ATP depletion. The post-mortem findings yielded images consistent with what has been reported for wildtype TDP-43 in familial and sporadic FTD (*6*, *7*). Loss of RNA-binding would be expected to expose one or more unstable interfaces within TDP-43's RRM domains including hydrophobic residues that mediate protein-RNA interaction (*62*) and whose exposure to nucleoplasm would recruit, and be stabilized by, HSP70 chaperone activity. HSP70's activity in the cytoplasm has been reported to be required to disassemble stress granules (*63*). HSP70's role in facilitating anisosome formation and maintenance adds an additional role for nuclear HSP70, which has been reported to facilitate delivery of aggregation-prone proteins to the nucleolus for proteasomal degradation during heat shock (*64*).

The TDP-43 anisosome was different from reentrant phase separation (RPS), a phenomenon identified in vitro using two purified components and in which moderate concentrations of a charged polymer (e.g., RNA) drive assembly of hollow droplets of an oppositely charged polymer (e.g., a positively charged polypeptide). In the RPS system the thickness of the shell changes in a concentration-dependent manner and superstoichiometric concentrations drive droplet disassembly (*65*, *66*). TDP-43 anisosomes, on the other hand, were formed from RNA-free TDP-43 and the ATP-dependent chaperone action of HSP70 variants.

Spherical shells similar to TDP-43 anisosomes have been reported in Drosophila germ granules, first reported as intranuclear spherical shells (*67*) and later shown to be gel-like (*68*). Furthermore, annular nuclear bodies, apparently containing both polyA-RNA and the RNA-binding protein SAM68, have also been reported (*69*) in degenerating motor neurons of SMNΔ7 mice, a model of spinal muscular atrophy type II. Matrin3, a protein encoded by an ALS-causing gene (*70*), forms round and apparently hollow nuclear droplets

when its second RNA-binding domain is removed, although it is not clear whether these droplets have liquid properties.

Abnormal aggregation of TDP-43 is nearly a universal feature in ALS and in FTD with ubiquitin positive inclusions (FTLD-U) (*2*, *71*), in hippocampal neurons of Alzheimer's disease [where it is correlated with ApoE4 alleles] (*72–74*), and in LATE, a dementia in the oldest individuals (*4*). TDP-43 aggregates have been reported in both the nucleus and the cytoplasm of neurons in postmortem FTD and AD nervous system tissues (*8*, *9*). ALS and FTD-causing TDP-43 mutants (such as P112H, K181E and K263E) have diminished RNA-binding and form anisosomes in cells. Where examined, acetylated, RNA-binding deficient TDP-43 is present in pathological TDP-43 aggregates (*16*). Here we have shown that TDP-43-containing anisosomes could be driven simply by altering the balance of ongoing acetylation/deacetylation or in neurons of the mammalian nervous system experiencing proteomic stress from transient proteasome inhibition. Furthermore, when ATP levels declined, as during the postmortem interval required for typical human nervous system tissue collection, TDP-43 anisosomes converted into aggregates. Taken together, the evidence suggests that anisosomes may be precursors of nuclear and/or cytoplasmic TDP-43 aggregates found in FTD, AD, LATE, and ALS (*7–9*, *36*, *37*).

Finally, our results suggest an essential partnership between TDP-43 and HSP70 chaperones in driving and maintaining TDP-43 phase separation and preventing TDP-43 aggregation. Future efforts are now needed to determine the identities of the TDP-43 acetylases and deacetylases that act on TDP-43. Similarly it remains to be seen whether there are age-dependent changes in acetylase/deacetylase activities that may synergize with the known age-dependent or drug-induced decline in proteasome (*32*, *33*) and nuclear import (*60*) activities to mediate stress-induced TDP-43 phase separation in age-related neurodegeneration (*4*, *6*, *8*, *9*, *36*, *37*, *71–74*) and chemotherapy-induced peripheral neuropathy (*75–77*).

Materials and methods

Plasmids

The information on all plasmids used in this paper is listed in supplementary table S1. In brief, the entry vectors (pHY135 and pHY195) were used as backbones for most of the lentiviral vectors, generated by traditional cloning method (using double-restriction digestion followed by ligation) or Gibson assembly (*78*). All plasmids in this manuscript will be deposited to Addgene. TDP-43^{2KQ}, and TDP-43^{mNLS,2KQ} cDNA was a gift from Dr. Todd Cohen. All other TDP-43 variants were constructed by H.Y. with the help of D. T., S. L., and S.V.S.

Cell culture, siRNA-knockdown, transient transfection and lentiviral transduction

Cell lines used in this paper are: HEK293T (ATCC: CRL-11268), U2OS (ATCC: HTB-96), SH-SY5Y (ATCC: CRL-2266), human iPS cell line CV-C – a gift from Eugene Yeo's group at UCSD (maintenance and differentiation will be described in a different section), and TDP-43 knockout HEK293T cells – a gift from Dr. Broder Schmidt (*79*). Routine maintenance of these model cell lines follows the standard protocol. In brief, U2OS and HEK293T cells were cultured in complete DMEM supplemented with 10% Fetal bovine serum (FBS). SH-SY5Y cells were cultured in DMEM/F12 supplemented with 10% FBS. HEK293T (TDP-43^{KO}) cell line (*79*) were cultured in DMEM supplemented with NEAA (Gibco, 11140050, 100X), Sodium Pyruvate (Gibco, 11360070, 100X) and 10% FBS.

Transient transfection was performed for HEK293T cells and U2OS cells at 60% confluency, by using transfection reagent TransIT X2 (Mirus, MIR6000) and the standard protocol posted on the product page of TransIT X2. In brief, serum free DMEM was used to dissolve DNA, and then TransIT X2 was added to the mix. After 15 min, the final mix was added dropwise to attached cells. The culture medium was changed after 12~24 hours post transfection.

To package lentivirus, a second-generation packaging system was used. Briefly, 0.5 million 293T cells were seeded per well in a 6-well plate. For lentiviral transfection, 2.5 μg of the lentiviral plasmid, 1.25 μg of pMD2.G and 0.625 μg of psPAX2 were inoculated to each well using the transIT-X2 transfection reagent. Culture medium was changed to fresh medium at 12~24 hours post transfection. Two days after transfection, the culture medium was filtered through a 0.45 μm syringe filter to generate the viral stock. 10-50 μg/mL protamine sulfate was added to the viral stock for transduction of U2OS or SH-SY5Y cells. After 24 hours of incubation with cells, the virus-containing media were removed and cells were passaged once before selection. Transduced cells are selected based on the selection marker encoded by the lentivirus. For U2OS, the concentrations of the antibiotics used for selection were 200 μg/mL for neomycin (G418, Gibco 10131035), 20 μg/mL for blasticidin (Gibco A1113903), and 1 μg/mL for puromycin (Gibco A1113803). For SH-SY5Y cells, the concentrations were 400 μg/mL for neomycin, 10 μg/mL for blasticidin and 3 μg/mL for puromycin. Detailed guides and protocols posted can be found on the Addgene website:

www.addgene.org/protocols/lentivirus-production/
www.addgene.org/guides/lentivirus/

The siRNA experiment used the same protocol and reagents as previously described by Melamed *et al.* (*13*).

Human induced pluripotent stem cell (iPSC) culture

Human iPSCs were grown in Matrigel-coated dishes (Corning, 354234) and mTeSR Plus media (StemCell Technologies,

05825) and passaged using Accutase (Innovative Cell Technologies, Inc., AT-104). ROCK inhibitor Y27632 (ApexBio, B1293-10) was used at 10 μM for 24 hours after every passaging or thawing.

Motor neuron differentiation from human iPSCs

The iPSCs were differentiated according to a modified version of Martinez *et al.* (*80*), based on the established strategy of dual-SMAD inhibition (*81*, *82*). iPSC dishes at 60-80% confluency were placed in 0.5XN2B27 media (DMEM/F12 + GlutaMAX media (Life Technologies, 10565-018) supplemented with 0.5X N2 supplement (Life Technologies, 17502-048), 0.5X B27 supplement (Life Technologies, 17504-044), 0.1 mM Ascorbic Acid (Sigma-Aldrich, A4544), and 1% PenStrep (Life Technologies, 15140-122)), which was supplemented with the different compounds throughout differentiation. On days 1-6, cells were fed daily with 0.5XN2B27 media in the presence of 1 μM Dorsomorphin (Tocris, 3093), 10 μM SB431542 (Tocris, 1614) and 3 μM CHIR99021 (Tocris, 4423). On day 7-18, cells were fed daily with 0.5X N2B27 in the presence of 1 μM Dorsomorphin, 10 μM SB431542, 0.2 μM Smoothened Agonist (SAG) (EMD Biosciences, 566660) and 1.5 μM Retinoic Acid (Sigma-Aldrich, R2625). On days 18-21, cells were fed every other day with 0.5XN2B27 in the presence of 0.2 μM SAG and 1.5 μM Retinoic Acid. On day 22 cells were passaged onto poly-Ornithine (Sigma-Aldrich, P3655)/poly-D-Lysine (Sigma-Aldrich, P6407)/Laminin (Sigma-Aldrich, L2020) coated plates, and on days 22-25 were fed with 0.5XN2B27 supplemented with 2 ng/μl of BDNF (R&D Systems, 248-BD), CTNF (R&D Systems, 257NT) and GDNF (R&D Systems, 212GD), in the presence of 2 μM DAPT (Tocris, 2634). From days 25 on, cells are fed every 2-3 days with 0.5XN2B27 supplemented with 2 ng/μl of BDNF, CTNF and GDNF. Cells were treated with 5 μM Ara-C (Sigma-Aldrich, C1768) for 48 hours to avoid expansion of glial cells.

Fluorescence activated cell sorting (FACS)

Before cell sorting or flowcytometry analysis, cells were trypsinized and resuspended in FACS buffer (1% FBS in PBS). Cell suspension was passed 40 μm strainer (Corning #352235) to form single cell suspension. The cells were loaded to SONY SH800S cell sorter to sort for single cell clones, or a population of defined clover fluorescence. For flowcytometry analyses, BD LSR-Fortessa was used.

Chemical treatments

Doxycycline (DOX Sigma-Aldrich, D9891) was used to induce gene expression via the TetON3G promoter. U2OS cell and SH-SY5Y cells were treated at 500 ng/mL final concentration of DOX. Trichostatin A (TSA, ApexBio, A8183) at 10 μg/mL and Vorinostat (SAHA, ApexBio, A4084) at 20 μM final concentrations were used to inhibit HDAC activity in HEK293T, U2OS and SH-SY5Y cells. Bortezomib (BTZ, ApexBio, A2614) at 2.5 μM final concentration was used to inhibit the proteasome function in SH-SY5Y cells and iPSC-derived motor neurons. RNA labeling was conducted by following the protocol of the kit (Thermo-Fisher, C10330). HSP70 inhibitor (VER155008, ApexBio, A4387) was used at 50 μM final concentration. To inhibit ATP production from mitochondria, 1 μM antimycin (Sigma-Aldrich, A8674) with 1 μM oligomycin (Sigma-Aldrich, O4876) (*83*) or 10 mM sodium azide (Sigma-Aldrich, S2002) (*84*) was used.

Fluorescence microscopy

Immunostaining and fluorescence images were acquired using a Zeiss LSM880 confocal microscope with Airyscan or a Leica SP8 confocal microscope with lightening deconvolution. Before imaging, cells were seeded in glass-bottom 8-well μ-slide (iBidi 80827). For live cell imaging, cells were incubated in Leibovitz's L-15 Medium supplemented with 10% FBS. For immunofluorescence, cells were first fixed with 4% PFA for 10 min at room temperature (RT), washed twice with PBS, and permeabilized by using 0.5% Triton X-100 in PBS. Then cells were incubated with blocking buffer (2% BSA, 0.1% Triton X-100 in PBS) for 30 min at RT. Primary antibodies were diluted in the blocking buffer, and cells were incubated with primary antibody over night at 4°C. Then cells were washed 3 times at RT by the washing buffer (0.1% Triton X-100 in PBS). Cells were incubated with secondary antibodies diluted in blocking buffer for 45 min at RT, covered from light. After the incubation with secondary antibodies, cells were washed 4 times at RT with washing buffer and stained with DAPI (Tocris #5748) at 1 μg/mL in PBS. After DAPI staining, cells were post-fixed by 4% PFA for 5 min at RT, and washed with PBS twice afterward, to immobilize the antibodies on their antigens. Then cells were mounted with ProLong Gold (Thermo-Fisher P10144) and 8mm coverslips (Electron Microscopy Sciences #72296-08).

Differential interference contrast (DIC) microscopy and complete extinction microscopy (CEM)

Both DIC and CEM were performed by using Nikon Eclipse Ti2-E microscope, equipped with 100x lens, TC-C-DICP-I intelligent linear polarizer (adjustable), a build-in linear polarizer in the base unit, CO_2 and temperature was maintained by Okolab H101 water jacket stage top chamber with lens heater, Okolab CO2 unit, and Oko-touch digital recorder. The sample temperature was recorded every 30s during the experiment. For DIC microscopy, the Nomarski prism was inserted to the base of the lens, and the adjustable polarizer was turned to obtain optimal contrast. For CEM, the Nomarski prism was pulled out (this is a critical step because the Nomarski prism generates artifact), and the microscope was set to a position where only two polarizers are in the light

pass. Images and movies were taken when the two linear polarizers are aligned at 0°, which allows maximum amount of light to pass. Then the adjustable linear polarizer was turned to a position where the least amount of light was detected by the camera. This position was defined as the complete extinction position.

Fluorescence recovery after photobleaching (FRAP) analysis and quantification

FRAP experiments on U2OS cells were performed on Zeiss LSM880 Airyscan microscope with 40x/1.2 Water objective at 37°C. The intensity of the fluorescent signal is controlled in the detection range through changing the laser power, digital gain and off-set. For the green channel, bleaching was conducted by a 488 nm line from an argon laser at ~80%-100% intensity with ~10-20 iterations. Fluorescence recovery was monitored at 2 s, 5 s or 10 s intervals for 3 min. In the focal-bleach experiment, roughly half of a particle is bleached, and then the distribution of the fluorescence within the bleached particle is determined over time. During the experiment cells were maintained in Leibovitz's L-15 medium (CO2 independent).

The FRAP data was quantified using Image J. The time series of the granule fluorescence intensity was calculated and the intensity of the background (area with no cells) was subtracted from the granule intensity. The intensity of the granule during the whole experiment was normalized to 1 before bleaching. An average of at least 10~20 particles per condition was used to calculate the mean and standard error. The averaged relative intensity and standard error were plotted to calculate the dynamics of the particles.

Immunoblotting

Sample collection: Cells were washed by ice cold PBS on ice before lysis using RIPA buffer. To remove DNA and RNA, and inhibit protease activity, RIPA buffer were supplemented with benzonase (Millipore, 101654) at 1 U/mL and protease inhibitor cocktail at 1X (100X cocktail from Thermo-Fisher, 78430). Cells were lysed with 200 µL per well for 6-well plate for 20 min and collected in 1.5 mL tubes. Lysates were centrifuged at 15000 g for 10 min. Supernatant were mixed with NuPAGE LDS sample buffer (Thermo-Fisher, NP0007). All procedures were performed on ice or at 4°C before boiling for 10 min at 95°C. SDS page, transfer, and blotting procedures were performed by following standard protocol. ECL substrates were used to visualize HRP-conjugated secondary antibody on the blot, and Biorad ChemiDoc system was used to capture the luminescent signals.

Co-Immunoprecipitation (co-IP)

HEK293T cells stably expressing HSPA1A$^{mRuby2\text{-}Flag}$ were induced to express TDP-43 variants (clover-tagged). After 2 days induction, cells were lysed with RIPA supplemented with protease inhibitors and 2 mM DTT. For some conditions, the lysis buffer was supplemented with 5 mM ATP. Cell lysate was then sonicated for 2 s at 35% amplitude for 2 times to shear the genomic DNA. Debris was pelleted by 10-min centrifugation at 20000g at 4°C. Anti-Flag M2 affinity gel (Sigma-Aldrich, A2220) was washed twice with complete RIPA buffer. To perform the co-IP experiment, 90% of the supernatant was added to 50 µL affinity gel and incubated at 4°C for 1 hour. Then, the supernatant was removed, and the gel was washed 3 times with complete RIPA buffer at 4°C. The protein on the gel was released by adding 2 x Laemmli SDS sample buffer and boiling for 10 min for immunoblotting. To eliminate the background of IgG heavy chain, anti-mouse light chain secondary antibody (Jackson Immunology #115-035-174) was used for immunoblotting.

Laboratory animals

Sprague-Dawley rats at five weeks of age and C57BL/6J mice at four months of age (The Jackson Laboratory, stock# 000664) were used for intravenous injection of BTZ (0.5mg/kg). Rat care, handling and experimental procedures were in accordance with Spanish legislation and the guidelines of the European Commission for the accommodation and care of laboratory animals. The experimental plan was preliminarily examined and approved by the Ethics Committee of the University of Cantabria. Mouse care, handling and experimental procedures were approved by the Institutional Animal Care and Use Committee of the University of California, San Diego. All the animals were housed in a limited access environment with a 12-hours light/dark cycle, where room temperature and relative humidity were set at 22 ± 2°C and 55 ± 10% respectively and there was free access to food and water. Animal sacrifice was performed under deep pentobarbital anesthesia (50 mg/kg) or in a euthanasia chamber containing 30% carbon dioxide.

Electron microscopy (EM) and ImmunoEM

U2OS cells were plated on coverslips and induced by doxycycline to express TDP-43 variants. Cells were fixed by 2% glutaraldehyde in 0.1 M sodium cacodylate (SC buffer) buffer for 60 min or longer at 4°C. After fixation, all procedures were carried out on ice. Fixed cells were washed with 0.1 M SC buffer five times and stained with 1% OsO_4 in 0.1M SC buffer for 45 min. Stained cells were then washed with 0.1 M SC buffer five times and MilliQ water for 2 times. Coverslips were placed in 2% uranyl acetate buffer for 45 min and then rinsed with Milli-Q water. Samples were serial dehydrated by immersion during 1 min in 20%, 50%, 70%, 90%, and two times in 100% ethanol and then two times in dry acetone . After dehydration, all steps were carried at room temperature (RT). Samples were then incubated with Ducurpan:Acetone

= 50/50 for 1 hour, and then two times for 1 hour in fresh 100% Durcupan. Coverslips were embedded in Durcupan resin, and cut into 60 nm ultrathin sections using a diamond knife. Sections were mounted on 300 mesh grids.

For immunoEM, U2OS cells containing TDP-43 anisosomes were fixed for 12 hours in 4% PFA in 0.1 M phosphate buffer, cryoprotected in sucrose, pelleted in 10% gelatin, and snap frozen in liquid nitrogen. Ultrathin cryosections (70–80 nm) were cut as previously described (Zheng *et al.*, 2004). Sections were picked up with a 1:1 mixture of 2.3 M sucrose and 2% methyl cellulose (15cp) as described by Liou *et al.* (1996) and transferred onto Formvar and carbon-coated copper grids. Immunolabeling was performed by a slight modification of the "Tokuyasu technique," (Tokuyasu, 1980). Briefly, grids were placed on 2% gelatin at 37°C for 20 min, rinsed with 0.15 M glycine in PBS and the sections were blocked using 1% cold water fish-skin gelatin. For immunogold labeling of TDP-43$^{2KQ\text{-}clover}$, sections were sequentially incubated for 2h with a mouse anti-GFP antibody (Clontech Living Colors A.V. JL-8), followed by a 12 nM gold conjugated goat anti-mouse IgG (Jackson Immunoresearch, 115-205-071) for 1 hour. Grids were then counterstained for 10 minutes in 0.4% uranyl acetate and 1.8% methyl cellulose on ice.

For immunoEM of TDP-43 in rat tissue, bortezomib-treated rats were subjected to transcardial perfusion under deep anesthesia with 3.7% paraformaldehyde in 0.1 M cacodylate buffer for 15 min at RT. Small tissue fragments of sensory ganglia were dissected and post-fixed in the same fixative solution for 4h at RT, washed in 0.1 M cacodylate buffer, dehydrated in increasing concentrations of methanol at −20°C, embedded in Lowicryl K4M at −20°C, and polymerized with ultraviolet irradiation. Ultrathin sections were mounted on Formvar coated nickel grids and sequentially incubated with 0.1 M glycine in PBS for 15 min, 3% BSA in PBS for 30 min, and the primary rabbit polyclonal anti-TDP-43 antibody (diluted 1:100 in 50 mM Tris–HCl, pH 7.6, containing 1% BSA and 0.1 M glycine) for 1 hour at 37°C. After washing, sections were incubated with the goat anti-rabbit IgG antibody coupled to 10-nm gold particles (BioCell, UK; diluted 1:50 in PBS containing 1% BSA). Following immunogold labeling, the grids were stained with lead citrate and 2% (w/v) uranyl acetate. As controls, ultrathin sections were treated as described above but with the primary antibody being omitted.

Imaging was carried out using a JEOL 1200 EX II electron microscope equipped with an Orius CCD Gatan camera and Gatan digital micrograph software (Gatan, Pleasanton, CA; University of California, San Diego, Cellular and Molecular Medicine Electron Microscopy Facility).

The calculation of average thickness and outer diameter of anisosomes in EM images: For each cross section of anisosomes, the thickness was measured as the average of the 8 yellow lines an example is shown in panel S4G. The error bars are the SEM of the 8 values. The average outer diameter of an anisosome was measured by the average of the 2 red lines.

Cryo-FIB milling and cryo-electron tomography

U2OS cells were dox-induced for 2-6 days and then seeded on glow-discharged Quantifoil grids (R1/4, Au 200-mesh grid, Electron Microscopy Sciences). The cells were then cultured for 24 hours with continued dox-induction. The grids were then manually blotted from the backside only (to remove excess media) and quickly plunge-frozen into liquid ethane/propane mixture using the custom-built vitrification device (Max Planck Institute for Biochemistry, Munich). From thereon, grids were always kept in cryogenic conditions. The grids were then clipped onto FIB-AutoGrids (ThermoFisher) for milling inside a Thermo Scientific Aquilos DualBeam. ~120-150 nm lamellae (~11 µm in width) were prepared in the Aquilos using rectangular milling patterns as previously described (*4*, *5*). Briefly, the coarse milling was performed with the ion beam current of 0.10-0.50 nA. The current was reduced to 10-50 pA for careful and slow fine milling.

The lamellae created on the grids were then stored in cryogenic conditions and eventually transferred to the transmission electron microscope (Titan Krios G3; ThermoFisher) using the AutoLoader (ThermoFisher). Tilt-images, in the form of cryo-transmission electron images, were acquired on the microscope operated at 300 kV and equipped with a Quantum post-column energy filter (Gatan). The images were recorded on a K2 Summit (Gatan) direct detector in the counting mode using the SerialEM software (*85*). The tilt-series acquisition parameters were as follows: tilt range: ± 60, magnification: 26000X-19500X, tilt increment: 3/2/1.5°, pixel size of 0.53-0.71 nm, target defocus: −5 µm. The images were recorded in the movie mode, the frames of the tilt-series images were motion corrected and dose-weighted using MotionCor2 (*86*). The tilt series were then aligned in IMOD using patch-tracking (*87*). No CTF correction was performed. The weighted back-projection method was used for the final tomographic reconstruction.

Proximity labeling and enrichment of biotinylated protein

Before the labeling experiment, U2OS cells were passaged in (Lys0, Arg0) or heavy (Lys8, Arg10) DMEM medium for 5 generations. U2OS cells were incubated with 500 µM biotin phenol (Iris-Biotech, 41994-02-9) containing medium for 30 min. Then 1 mM hydrogen peroxide was added to the medium to activate APEX reaction for 1 min, followed by immediate quenching of reaction with ice-cold quenching buffer (1xPBS, 10 mM sodium azide, 10 mM sodium ascorbate, 5 mM

Trolox). After washing with cold quenching buffer for three times, the cells were collected from plates with scrapers.

Cells were lysed in lysis buffer (100 mM NaPO4, PH 8.0, 8 M Urea, 0.05% SDS, 10 mM sodium azide, 10 mM sodium ascorbate, 5 mM Trolox supplemented with 500 unit benzonase to remove DNA and RNA) and rotated at room temperature for 15 min. Then SDS was increased to 1% and sonication was performed in a water bath sonicator for 10 min. Protein concentration was measured using 2-D quant kit (GE healthcare, 80648356), by following manufacturer's instructions. The denatured proteins were reduced with 5 mM TCEP and alkylated with 10 mM Iodoacetamide. Equal amount of proteins from light and heavy group were mixed together and then the mixed cell lysates were diluted with equal volume of ddH2O to reduce the concentration of urea to 4 M and SDS to 0.5%. The samples were incubated with streptavidin magnetic beads at 4°C overnight. After four washes with wash buffer (100 mM NaPO4, PH 8.0, 4 M Urea), the beads were resuspended in 100 mM TEAB, 2 M Urea supplemented with 10 ng/μL Trypsin, 5 ng/μL Lys-C for digestion overnight. The digested products were collected and added with 1% formic acid (final concentration) for LC-MS/MS analysis.

Liquid chromatography-Mass spectrometry analysis

LC-MS/MS was conducted on Orbitrap Elite Hybrid Mass Spectrometer interfaced with a nano-flow HPLC Easy II. Digested peptides were loaded onto a 100 μm × 15 cm analytical column packed with 3 μm, 120 Å C18 resin (Phenomenex 04A-4758). The peptides were separated over a 90-min linear gradient from 0% buffer B (95% acetonitrile, 0.1% formic acid), 100% buffer A (5% acetonitrile, 0.1% formic acid) to 30% buffer B, followed by a 10-min gradient from 27% to 80% buffer B, then maintaining at 80% buffer B for 20 min. The flow rate was 300 nL/min. The MS parameters were: R = 140,000 in full scan, R = 7,500 in HCD MS2 scan; the 10 most intense ions in each full scan were selected for HCD dissociation; the AGC targets were 1e6 for FTMS full scan and 5e4 for MS2; minimal signal threshold for MS2 was 5e3; precursors having a charge state of +1, or unassigned were excluded; normalized collision energy was set to 30; dynamic exclusion was on.

Quantitative mass spectrometry data analysis

The raw data was processed by pParse (*88*), and co-eluting precursor ions were excluded. MS1 and MS2 data were searched using pFind 3 (*89*) against a complete human protein database downloaded from Uniprot with the addition of APEX2 and clover protein sequence. The settings of pFind 3 are: open search mode; 3 missed cleavage sites for trypsin digestion; peptide length 6-25 aa; fixed modification was carboxymethylation on Cys (58.0054 Da); variable modifications were oxidation on Met (15.9949 Da) and acetylation on N-term (42.0105 Da). The search results are filtered with less than 10 ppm mass deviation for precursor ions and 20 ppm for fragment ions, FDR < 0.01 at peptide level. The identified spectra were used for quantification with pQuant (*90*) with the setting of using 200 MS1 scans before and after the spectra corresponding to identified spectra for searching the chromatography peaks and allowing 2 holes in the chromatography peak and the intensity of ion within 10 ppm mass deviation was used.

The median value of the ratio of light to heavy peptides from each protein was used as the ratio of the protein. The ratios of each protein from two forward labeling groups and one reverse labeling group were used to calculate P-value through one sample *t* test. The volcano plot was generated with R package.

Mathematical modeling

In building this model of TDP43 mutant phase separation, we initially considered whether the TDP43 mutant dimer could form annuli on its own by phase separating from the solvent and the RNA. While we observed exclusion of the RNA from the phase separated TDP43, we were unable to observe annuli formation by the TDP43 dimer, as shown in the Supplementary Material. Using our previous work (*56*), we knew that annulus-like pattern formation occurs when two components phase separate together, resulting in the proposal of Y. Further, when building this model to incorporate Y, four different sets of parameters needed to be considered: diffusion coefficients, χ-values (de-mixing energy), binding rates, and initial conditions.

We used an established theoretical diffusion coefficient values for proteins, RNAs and the subsequent complexes they formed based on a comparison of their molecular weights (*56*). The code can be downloaded from this link: https://doi.org/10.5281/zenodo.4299457. We assumed, for simplicity, a lack of folding that would influence the diffusion coefficient. The molecular weight of the protein used in Gasior, Zhao *et al.* (*56*) is similar to that of TDP-43, but the size of the RNA that can exist within the nucleus can vary drastically 10^2-10^5). For simplicity, we used a value closer to the lower end of this range and thus modeled RNA to be 8x the molecular weight of the TDP-43 mutant, which is reflected in the diffusion coefficient. Further, because there are two monomers that are used to create the dimer, the TDP-43 mutant dimer has a diffusion coefficient half as large as the TDP43 mutant monomer. The code can be downloaded from this link: https://doi.org/10.5281/zenodo.4287615.

Statistics and data reproducibility

Except for the quantitative analyses for the proteomic data, student *t* test (comparing two groups) and one-way ANOVA

(comparing three groups or more) were used to calculate significance, and $P < 0.05$ is considered statistically significant.

Each experiment was conducted at least three times or with at least three biological replicates.

REFERENCES AND NOTES

1. J. P. Taylor, R. H. Brown Jr., D. W. Cleveland, Decoding ALS: From genes to mechanism. *Nature* **539**, 197–206 (2016). doi:10.1038/nature20413 Medline
2. M. Neumann, D. M. Sampathu, L. K. Kwong, A. C. Truax, M. C. Micsenyi, T. T. Chou, J. Bruce, T. Schuck, M. Grossman, C. M. Clark, L. F. McCluskey, B. L. Miller, E. Masliah, I. R. Mackenzie, H. Feldman, W. Feiden, H. A. Kretzschmar, J. Q. Trojanowski, V. M.-Y. Lee, Ubiquitinated TDP-43 in frontotemporal lobar degeneration and amyotrophic lateral sclerosis. *Science* **314**, 130–133 (2006). doi:10.1126/science.1134108 Medline
3. C. Amador-Ortiz, W.-L. Lin, Z. Ahmed, D. Personett, P. Davies, R. Duara, N. R. Graff-Radford, M. L. Hutton, D. W. Dickson, TDP-43 immunoreactivity in hippocampal sclerosis and Alzheimer's disease. *Ann. Neurol.* **61**, 435–445 (2007). doi:10.1002/ana.21154 Medline
4. P. T. Nelson, D. W. Dickson, J. Q. Trojanowski, C. R. Jack, P. A. Boyle, K. Arfanakis, R. Rademakers, I. Alafuzoff, J. Attems, C. Brayne, I. T. S. Coyle-Gilchrist, H. C. Chui, D. W. Fardo, M. E. Flanagan, G. Halliday, S. R. K. Hokkanen, S. Hunter, G. A. Jicha, Y. Katsumata, C. H. Kawas, C. D. Keene, G. G. Kovacs, W. A. Kukull, A. I. Levey, N. Makkinejad, T. J. Montine, S. Murayama, M. E. Murray, S. Nag, R. A. Rissman, W. W. Seeley, R. A. Sperling, C. L. White Iii, L. Yu, J. A. Schneider, Limbic-predominant age-related TDP-43 encephalopathy (LATE): Consensus working group report. *Brain* **142**, 1503–1527 (2019). doi:10.1093/brain/awz099 Medline
5. M. Polymenidou, C. Lagier-Tourenne, K. R. Hutt, S. C. Huelga, J. Moran, T. Y. Liang, S.-C. Ling, E. Sun, E. Wancewicz, C. Mazur, H. Kordasiewicz, Y. Sedaghat, J. P. Donohue, L. Shiue, C. F. Bennett, G. W. Yeo, D. W. Cleveland, Long pre-mRNA depletion and RNA missplicing contribute to neuronal vulnerability from loss of TDP-43. *Nat. Neurosci.* **14**, 459–468 (2011). doi:10.1038/nn.2779 Medline
6. I. R. Mackenzie, M. Neumann, A. Baborie, D. M. Sampathu, D. Du Plessis, E. Jaros, R. H. Perry, J. Q. Trojanowski, D. M. A. Mann, V. M. Y. Lee, A harmonized classification system for FTLD-TDP pathology. *Acta Neuropathol.* **122**, 111–113 (2011). doi:10.1007/s00401-011-0845-8 Medline
7. I. R. Mackenzie, M. Neumann, Reappraisal of TDP-43 pathology in FTLD-U subtypes. *Acta Neuropathol.* **134**, 79–96 (2017). doi:10.1007/s00401-017-1716-8 Medline
8. M. Neumann, I. R. Mackenzie, N. J. Cairns, P. J. Boyer, W. R. Markesbery, C. D. Smith, J. P. Taylor, H. A. Kretzschmar, V. E. Kimonis, M. S. Forman, TDP-43 in the ubiquitin pathology of frontotemporal dementia with VCP gene mutations. *J. Neuropathol. Exp. Neurol.* **66**, 152–157 (2007). doi:10.1097/nen.0b013e31803020b9 Medline
9. S. O. Tomé, R. Vandenberghe, S. Ospitalieri, E. Van Schoor, T. Tousseyn, M. Otto, C. A. F. von Arnim, D. R. Thal, Distinct molecular patterns of TDP-43 pathology in Alzheimer's disease: Relationship with clinical phenotypes. *Acta Neuropathol. Commun.* **8**, 61 (2020). doi:10.1186/s40478-020-00934-5 Medline
10. F. Gasset-Rosa, S. Lu, H. Yu, C. Chen, Z. Melamed, L. Guo, J. Shorter, S. Da Cruz, D. W. Cleveland, Cytoplasmic TDP-43 De-mixing Independent of Stress Granules Drives Inhibition of Nuclear Import, Loss of Nuclear TDP-43, and Cell Death. *Neuron* **102**, 339–357.e7 (2019). doi:10.1016/j.neuron.2019.02.038 Medline
11. J. R. Klim, L. A. Williams, F. Limone, I. Guerra San Juan, B. N. Davis-Dusenbery, D. A. Mordes, A. Burberry, M. J. Steinbaugh, K. K. Gamage, R. Kirchner, R. Moccia, S. H. Cassel, K. Chen, B. J. Wainger, C. J. Woolf, K. Eggan, ALS-implicated protein TDP-43 sustains levels of STMN2, a mediator of motor neuron growth and repair. *Nat. Neurosci.* **22**, 167–179 (2019). doi:10.1038/s41593-018-0300-4 Medline
12. J. P. Ling, O. Pletnikova, J. C. Troncoso, P. C. Wong, TDP-43 repression of nonconserved cryptic exons is compromised in ALS-FTD. *Science* **349**, 650–655 (2015). doi:10.1126/science.aab0983 Medline
13. Z. Melamed, J. López-Erauskin, M. W. Baughn, O. Zhang, K. Drenner, Y. Sun, F. Freyermuth, M. A. McMahon, M. S. Beccari, J. W. Artates, T. Ohkubo, M. Rodriguez, N. Lin, D. Wu, C. F. Bennett, F. Rigo, S. Da Cruz, J. Ravits, C. Lagier-Tourenne, D. W. Cleveland, Premature polyadenylation-mediated loss of stathmin-2 is a hallmark of TDP-43-dependent neurodegeneration. *Nat. Neurosci.* **22**, 180–190 (2019). doi:10.1038/s41593-018-0293-z Medline
14. A. N. Coyne, I. Lorenzini, C.-C. Chou, M. Torvund, R. S. Rogers, A. Starr, B. L. Zaepfel, J. Levy, J. Johannesmeyer, J. C. Schwartz, H. Nishimune, K. Zinsmaier, W. Rossoll, R. Sattler, D. C. Zarnescu, Post-transcriptional Inhibition of Hsc70-4/HSPA8 Expression Leads to Synaptic Vesicle Cycling Defects in Multiple Models of ALS. *Cell Rep.* **21**, 110–125 (2017). doi:10.1016/j.celrep.2017.09.028 Medline
15. K. Miskiewicz, L. E. Jose, W. M. Yeshaw, J. S. Valadas, J. Swerts, S. Munck, F. Feiguin, B. Dermaut, P. Verstreken, HDAC6 is a Bruchpilot deacetylase that facilitates neurotransmitter release. *Cell Rep.* **8**, 94–102 (2014). doi:10.1016/j.celrep.2014.05.051 Medline
16. T. J. Cohen, A. W. Hwang, C. R. Restrepo, C.-X. Yuan, J. Q. Trojanowski, V. M. Y. Lee, An acetylation switch controls TDP-43 function and aggregation propensity. *Nat. Commun.* **6**, 5845 (2015). doi:10.1038/ncomms6845 Medline
17. S. F. Banani, H. O. Lee, A. A. Hyman, M. K. Rosen, Biomolecular condensates: Organizers of cellular biochemistry. *Nat. Rev. Mol. Cell Biol.* **18**, 285–298 (2017). doi:10.1038/nrm.2017.7 Medline
18. W. T. Snead, A. S. Gladfelter, The Control Centers of Biomolecular Phase Separation: How Membrane Surfaces, PTMs, and Active Processes Regulate Condensation. *Mol. Cell* **76**, 295–305 (2019). doi:10.1016/j.molcel.2019.09.016 Medline
19. C. P. Brangwynne, C. R. Eckmann, D. S. Courson, A. Rybarska, C. Hoege, J. Gharakhani, F. Jülicher, A. A. Hyman, Germline P granules are liquid droplets that localize by controlled dissolution/condensation. *Science* **324**, 1729–1732 (2009). doi:10.1126/science.1172046 Medline
20. A. Jain, R. D. Vale, RNA phase transitions in repeat expansion disorders. *Nature* **546**, 243–247 (2017). doi:10.1038/nature22386 Medline
21. J. B. Woodruff, B. Ferreira Gomes, P. O. Widlund, J. Mahamid, A. Honigmann, A. A. Hyman, The Centrosome Is a Selective Condensate that Nucleates Microtubules by Concentrating Tubulin. *Cell* **169**, 1066–1077.e10 (2017). doi:10.1016/j.cell.2017.05.028 Medline
22. H. B. Schmidt, D. Görlich, Transport Selectivity of Nuclear Pores, Phase Separation, and Membraneless Organelles. *Trends Biochem. Sci.* **41**, 46–61 (2016). doi:10.1016/j.tibs.2015.11.001 Medline
23. D. Hnisz, K. Shrinivas, R. A. Young, A. K. Chakraborty, P. A. Sharp, A Phase Separation Model for Transcriptional Control. *Cell* **169**, 13–23 (2017). doi:10.1016/j.cell.2017.02.007 Medline
24. M. Feric, N. Vaidya, T. S. Harmon, D. M. Mitrea, L. Zhu, T. M. Richardson, R. W. Kriwacki, R. V. Pappu, C. P. Brangwynne, Coexisting Liquid Phases Underlie Nucleolar Subcompartments. *Cell* **165**, 1686–1697 (2016). doi:10.1016/j.cell.2016.04.047 Medline
25. J. A. West, M. Mito, S. Kurosaka, T. Takumi, C. Tanegashima, T. Chujo, K. Yanaka, R. E. Kingston, T. Hirose, C. Bond, A. Fox, S. Nakagawa, Structural, super-resolution microscopy analysis of paraspeckle nuclear body organization. *J. Cell Biol.* **214**, 817–830 (2016). doi:10.1083/jcb.201601071 Medline
26. C. P. Brangwynne, T. J. Mitchison, A. A. Hyman, Active liquid-like behavior of nucleoli determines their size and shape in Xenopus laevis oocytes. *Proc. Natl. Acad. Sci. U.S.A.* **108**, 4334–4339 (2011). doi:10.1073/pnas.1017150108 Medline
27. A. Putnam, M. Cassani, J. Smith, G. Seydoux, A gel phase promotes condensation of liquid P granules in Caenorhabditis elegans embryos. *Nat. Struct. Mol. Biol.* **26**, 220–226 (2019). doi:10.1038/s41594-019-0193-2 Medline
28. L. D. Gallego, M. Schneider, C. Mittal, A. Romanauska, R. M. Gudino Carrillo, T. Schubert, B. F. Pugh, A. Köhler, Phase separation directs ubiquitination of gene-body nucleosomes. *Nature* **579**, 592–597 (2020). doi:10.1038/s41586-020-2097-z Medline
29. H. B. Schmidt, R. Rohatgi, In Vivo Formation of Vacuolated Multi-phase Compartments Lacking Membranes. *Cell Rep.* **16**, 1228–1236 (2016). doi:10.1016/j.celrep.2016.06.088 Medline
30. C. Wang, Y. Duan, G. Duan, Q. Wang, K. Zhang, X. Deng, B. Qian, J. Gu, Z. Ma, S. Zhang, L. Guo, C. Liu, Y. Fang, Stress Induces Dynamic, Cytotoxicity-Antagonizing TDP-43 Nuclear Bodies via Paraspeckle LncRNA NEAT1-Mediated Liquid-Liquid Phase Separation. *Mol. Cell* **79**, 443–458.e7 (2020). doi:10.1016/j.molcel.2020.06.019 Medline
31. J. Wang, J.-M. Choi, A. S. Holehouse, H. O. Lee, X. Zhang, M. Jahnel, S. Maharana, R. Lemaitre, A. Pozniakovsky, D. Drechsel, I. Poser, R. V. Pappu, S. Alberti, A. A. Hyman, A Molecular Grammar Governing the Driving Forces for Phase Separation of Prion-like RNA Binding Proteins. *Cell* **174**, 688–699.e16 (2018). doi:10.1016/j.cell.2018.06.006 Medline

32. E. Kelmer Sacramento, J. M. Kirkpatrick, M. Mazzetto, M. Baumgart, A. Bartolome, S. Di Sanzo, C. Caterino, M. Sanguanini, N. Papaevgeniou, M. Lefaki, D. Childs, S. Bagnoli, E. Terzibasi Tozzini, D. Di Fraia, N. Romanov, P. H. Sudmant, W. Huber, N. Chondrogianni, M. Vendruscolo, A. Cellerino, A. Ori, Reduced proteasome activity in the aging brain results in ribosome stoichiometry loss and aggregation. *Mol. Syst. Biol.* **16**, e9596 (2020). doi:10.15252/msb.20209596 Medline
33. I. Saez, D. Vilchez, The Mechanistic Links Between Proteasome Activity, Aging and Age-related Diseases. *Curr. Genomics* **15**, 38–51 (2014). doi:10.2174/1389202915011403061133344 Medline
34. T. Afroz, E.-M. Hock, P. Ernst, C. Foglieni, M. Jambeau, L. A. B. Gilhespy, F. Laferriere, Z. Maniecka, A. Plückthun, P. Mittl, P. Paganetti, F. H. T. Allain, M. Polymenidou, Functional and dynamic polymerization of the ALS-linked protein TDP-43 antagonizes its pathologic aggregation. *Nat. Commun.* **8**, 45 (2017). doi:10.1038/s41467-017-00062-0 Medline
35. A. Wang, A. E. Conicella, H. B. Schmidt, E. W. Martin, S. N. Rhoads, A. N. Reeb, A. Nourse, D. Ramirez Montero, V. H. Ryan, R. Rohatgi, F. Shewmaker, M. T. Naik, T. Mittag, Y. M. Ayala, N. L. Fawzi, A single N-terminal phosphomimic disrupts TDP-43 polymerization, phase separation, and RNA splicing. *EMBO J.* **37**, ••• (2018). doi:10.15252/embj.201797452 Medline
36. F. Moreno, G. D. Rabinovici, A. Karydas, Z. Miller, S. C. Hsu, A. Legati, J. Fong, D. Schonhaut, H. Esselmann, C. Watson, M. L. Stephens, J. Kramer, J. Wiltfang, W. W. Seeley, B. L. Miller, G. Coppola, L. T. Grinberg, A novel mutation P112H in the TARDBP gene associated with frontotemporal lobar degeneration without motor neuron disease and abundant neuritic amyloid plaques. *Acta Neuropathol. Commun.* **3**, 19 (2015). doi:10.1186/s40478-015-0190-6 Medline
37. H. J. Chen, S. D. Topp, H. S. Hui, E. Zacco, M. Katarya, C. McLoughlin, A. King, B. N. Smith, C. Troakes, A. Pastore, C. E. Shaw, RRM adjacent TARDBP mutations disrupt RNA binding and enhance TDP-43 proteinopathy. *Brain* **142**, 3753–3770 (2019). doi:10.1093/brain/awz313 Medline
38. G. G. Kovacs, J. R. Murrell, S. Horvath, L. Haraszti, K. Majtenyi, M. J. Molnar, H. Budka, B. Ghetti, S. Spina, TARDBP variation associated with frontotemporal dementia, supranuclear gaze palsy, and chorea. *Mov. Disord.* **24**, 1842–1847 (2009). doi:10.1002/mds.22697 Medline
39. A. C. Elden, H.-J. Kim, M. P. Hart, A. S. Chen-Plotkin, B. S. Johnson, X. Fang, M. Armakola, F. Geser, R. Greene, M. M. Lu, A. Padmanabhan, D. Clay-Falcone, L. McCluskey, L. Elman, D. Juhr, P. J. Gruber, U. Rüb, G. Auburger, J. Q. Trojanowski, V. M.-Y. Lee, V. M. Van Deerlin, N. M. Bonini, A. D. Gitler, Ataxin-2 intermediate-length polyglutamine expansions are associated with increased risk for ALS. *Nature* **466**, 1069–1075 (2010). doi:10.1038/nature09320 Medline
40. N. Vo, R. H. Goodman, CREB-binding protein and p300 in transcriptional regulation. *J. Biol. Chem.* **276**, 13505–13508 (2001). doi:10.1074/jbc.R000025200 Medline
41. T. J. Cohen, V. M. Lee, J. Q. Trojanowski, TDP-43 functions and pathogenic mechanisms implicated in TDP-43 proteinopathies. *Trends Mol. Med.* **17**, 659–667 (2011). doi:10.1016/j.molmed.2011.06.004 Medline
42. B. N. Flores, X. Li, A. M. Malik, J. Martinez, A. A. Beg, S. J. Barmada, An Intramolecular Salt Bridge Linking TDP43 RNA Binding, Protein Stability, and TDP43-Dependent Neurodegeneration. *Cell Rep.* **27**, 1133–1150.e8 (2019). doi:10.1016/j.celrep.2019.03.093 Medline
43. G. Pelzl, A. Hauser, Birefringence and phase transitions in liquid crystals. *Phase Transit.* **37**, 33–62 (1991). doi:10.1080/01411599108203447
44. R. Oldenbourg, Polarized light microscopy: Principles and practice. *Cold Spring Harb. Protoc.* **2013**, pdb.top078600 (2013). doi:10.1101/pdb.top078600 Medline
45. C. Reyes Mateo, A. Ulises Acuña, J. C. Brochon, Liquid-crystalline phases of cholesterol/lipid bilayers as revealed by the fluorescence of trans-parinaric acid. *Biophys. J.* **68**, 978–987 (1995). doi:10.1016/S0006-3495(95)80273-0 Medline
46. K. Liu, D. Chen, A. Marcozzi, L. Zheng, J. Su, D. Pesce, W. Zajaczkowski, A. Kolbe, W. Pisula, K. Müllen, N. A. Clark, A. Herrmann, Thermotropic liquid crystals from biomacromolecules. *Proc. Natl. Acad. Sci. U.S.A.* **111**, 18596–18600 (2014). doi:10.1073/pnas.1421257111 Medline
47. O. Rog, S. Köhler, A. F. Dernburg, The synaptonemal complex has liquid crystalline properties and spatially regulates meiotic recombination factors. *eLife* **6**, e21455 (2017). doi:10.7554/eLife.21455 Medline
48. Y. M. Ayala, L. De Conti, S. E. Avendaño-Vázquez, A. Dhir, M. Romano, A. D'Ambrogio, J. Tollervey, J. Ule, M. Baralle, E. Buratti, F. E. Baralle, TDP-43 regulates its mRNA levels through a negative feedback loop. *EMBO J.* **30**, 277–288 (2011). doi:10.1038/emboj.2010.310 Medline
49. S. Saha, C. A. Weber, M. Nousch, O. Adame-Arana, C. Hoege, M. Y. Hein, E. Osborne-Nishimura, J. Mahamid, M. Jahnel, L. Jawerth, A. Pozniakovski, C. R. Eckmann, F. Jülicher, A. A. Hyman, Polar Positioning of Phase-Separated Liquid Compartments in Cells Regulated by an mRNA Competition Mechanism. *Cell* **166**, 1572–1584.e16 (2016). doi:10.1016/j.cell.2016.08.006 Medline
50. D. Bracha, M. T. Walls, M.-T. Wei, L. Zhu, M. Kurian, J. L. Avalos, J. E. Toettcher, C. P. Brangwynne, Mapping Local and Global Liquid Phase Behavior in Living Cells Using Photo-Oligomerizable Seeds. *Cell* **175**, 1467–1480.e13 (2018). doi:10.1016/j.cell.2018.10.048 Medline
51. J. D. Vargas, E. M. Hatch, D. J. Anderson, M. W. Hetzer, Transient nuclear envelope rupturing during interphase in human cancer cells. *Nucleus* **3**, 88–100 (2012). doi:10.4161/nucl.18954 Medline
52. A. Patel, H. O. Lee, L. Jawerth, S. Maharana, M. Jahnel, M. Y. Hein, S. Stoynov, J. Mahamid, S. Saha, T. M. Franzmann, A. Pozniakovski, I. Poser, N. Maghelli, L. A. Royer, M. Weigert, E. W. Myers, S. Grill, D. Drechsel, A. A. Hyman, S. Alberti, A Liquid-to-Solid Phase Transition of the ALS Protein FUS Accelerated by Disease Mutation. *Cell* **162**, 1066–1077 (2015). doi:10.1016/j.cell.2015.07.047 Medline
53. A. E. Conicella, G. L. Dignon, G. H. Zerze, H. B. Schmidt, A. M. D'Ordine, Y. C. Kim, R. Rohatgi, Y. M. Ayala, J. Mittal, N. L. Fawzi, TDP-43 α-helical structure tunes liquid-liquid phase separation and function. *Proc. Natl. Acad. Sci. U.S.A.* **117**, 5883–5894 (2020). doi:10.1073/pnas.1912055117 Medline
54. M. Mompeán, V. Romano, D. Pantoja-Uceda, C. Stuani, F. E. Baralle, E. Buratti, D. V. Laurents, Point mutations in the N-terminal domain of transactive response DNA-binding protein 43 kDa (TDP-43) compromise its stability, dimerization, and functions. *J. Biol. Chem.* **292**, 11992–12006 (2017). doi:10.1074/jbc.M117.775965 Medline
55. Y. Shiina, K. Arima, H. Tabunoki, J. Satoh, TDP-43 dimerizes in human cells in culture. *Cell. Mol. Neurobiol.* **30**, 641–652 (2010). doi:10.1007/s10571-009-9489-9 Medline
56. K. Gasior, J. Zhao, G. McLaughlin, M. G. Forest, A. S. Gladfelter, J. Newby, Partial demixing of RNA-protein complexes leads to intradroplet patterning in phase-separated biological condensates. *Phys. Rev. E* **99**, 012411 (2019). doi:10.1103/PhysRevE.99.012411 Medline
57. D. R. Palleros, W. J. Welch, A. L. Fink, Interaction of hsp70 with unfolded proteins: Effects of temperature and nucleotides on the kinetics of binding. *Proc. Natl. Acad. Sci. U.S.A.* **88**, 5719–5723 (1991). doi:10.1073/pnas.88.13.5719 Medline
58. R. Rosenzweig, N. B. Nillegoda, M. P. Mayer, B. Bukau, The Hsp70 chaperone network. *Nat. Rev. Mol. Cell Biol.* **20**, 665–680 (2019). doi:10.1038/s41580-019-0133-3 Medline
59. D. S. Williamson, J. Borgognoni, A. Clay, Z. Daniels, P. Dokurno, M. J. Drysdale, N. Foloppe, G. L. Francis, C. J. Graham, R. Howes, A. T. Macias, J. B. Murray, R. Parsons, T. Shaw, A. E. Surgenor, L. Terry, Y. Wang, M. Wood, A. J. Massey, Novel adenosine-derived inhibitors of 70 kDa heat shock protein, discovered through structure-based design. *J. Med. Chem.* **52**, 1510–1513 (2009). doi:10.1021/jm801627a Medline
60. M. A. D'Angelo, M. Raices, S. H. Panowski, M. W. Hetzer, Age-dependent deterioration of nuclear pore complexes causes a loss of nuclear integrity in postmitotic cells. *Cell* **136**, 284–295 (2009). doi:10.1016/j.cell.2008.11.037 Medline
61. B. A. Gibson, L. K. Doolittle, M. W. G. Schneider, L. E. Jensen, N. Gamarra, L. Henry, D. W. Gerlich, S. Redding, M. K. Rosen, Organization of Chromatin by Intrinsic and Regulated Phase Separation. *Cell* **179**, 470–484.e21 (2019). doi:10.1016/j.cell.2019.08.037 Medline
62. P. J. Lukavsky, D. Daujotyte, J. R. Tollervey, J. Ule, C. Stuani, E. Buratti, F. E. Baralle, F. F. Damberger, F. H.-T. Allain, Molecular basis of UG-rich RNA recognition by the human splicing factor TDP-43. *Nat. Struct. Mol. Biol.* **20**, 1443–1449 (2013). doi:10.1038/nsmb.2698 Medline
63. M. Ganassi, D. Mateju, I. Bigi, L. Mediani, I. Poser, H. O. Lee, S. J. Seguin, F. F. Morelli, J. Vinet, G. Leo, O. Pansarasa, C. Cereda, A. Poletti, S. Alberti, S. Carra, A Surveillance Function of the HSPB8-BAG3-HSP70 Chaperone Complex Ensures Stress Granule Integrity and Dynamism. *Mol. Cell* **63**, 796–810 (2016). doi:10.1016/j.molcel.2016.07.021 Medline
64. F. Frottin, F. Schueder, S. Tiwary, R. Gupta, R. Körner, T. Schlichthaerle, J. Cox, R.

Jungmann, F. U. Hartl, M. S. Hipp, The nucleolus functions as a phase-separated protein quality control compartment. *Science* **365**, 342–347 (2019). doi:10.1126/science.aaw9157 Medline
65. I. Alshareedah, M. M. Moosa, M. Raju, D. A. Potoyan, P. R. Banerjee, Phase transition of RNA-protein complexes into ordered hollow condensates. *Proc. Natl. Acad. Sci. U.S.A.* **117**, 15650–15658 (2020). doi:10.1073/pnas.1922365117 Medline
66. P. R. Banerjee, A. N. Milin, M. M. Moosa, P. L. Onuchic, A. A. Deniz, Reentrant Phase Transition Drives Dynamic Substructure Formation in Ribonucleoprotein Droplets. *Angew. Chem. Int. Ed.* **56**, 11354–11359 (2017). doi:10.1002/anie.201703191 Medline
67. K. Illmensee, A. P. Mahowald, M. R. Loomis, The ontogeny of germ plasm during oogenesis in Drosophila. *Dev. Biol.* **49**, 40–65 (1976). doi:10.1016/0012-1606(76)90257-8 Medline
68. K. E. Kistler, T. Trcek, T. R. Hurd, R. Chen, F.-X. Liang, J. Sall, M. Kato, R. Lehmann, Phase transitioned nuclear Oskar promotes cell division of *Drosophila* primordial germ cells. *eLife* **7**, e37949 (2018). doi:10.7554/eLife.37949 Medline
69. J. O. Narcís, O. Tapia, O. Tarabal, L. Piedrafita, J. Calderó, M. T. Berciano, M. Lafarga, Accumulation of poly(A) RNA in nuclear granules enriched in Sam68 in motor neurons from the SMNΔ7 mouse model of SMA. *Sci. Rep.* **8**, 9646 (2018). doi:10.1038/s41598-018-27821-3 Medline
70. M. C. Gallego-Iradi, H. Strunk, A. M. Crown, R. Davila, H. Brown, E. Rodriguez-Lebron, D. R. Borchelt, N-terminal sequences in matrin 3 mediate phase separation into droplet-like structures that recruit TDP43 variants lacking RNA binding elements. *Lab. Invest.* **99**, 1030–1040 (2019). doi:10.1038/s41374-019-0260-7 Medline
71. S. C. Ling, M. Polymenidou, D. W. Cleveland, Converging mechanisms in ALS and FTD: Disrupted RNA and protein homeostasis. *Neuron* **79**, 416–438 (2013). doi:10.1016/j.neuron.2013.07.033 Medline
72. J. L. Robinson, E. B. Lee, S. X. Xie, L. Rennert, E. Suh, C. Bredenberg, C. Caswell, V. M. Van Deerlin, N. Yan, A. Yousef, H. I. Hurtig, A. Siderowf, M. Grossman, C. T. McMillan, B. Miller, J. E. Duda, D. J. Irwin, D. Wolk, L. Elman, L. McCluskey, A. Chen-Plotkin, D. Weintraub, S. E. Arnold, J. Brettschneider, V. M.-Y. Lee, J. Q. Trojanowski, Neurodegenerative disease concomitant proteinopathies are prevalent, age-related and APOE4-associated. *Brain* **141**, 2181–2193 (2018). doi:10.1093/brain/awy146 Medline
73. H. S. Yang, L. Yu, C. C. White, L. B. Chibnik, J. P. Chhatwal, R. A. Sperling, D. A. Bennett, J. A. Schneider, P. L. De Jager, Evaluation of TDP-43 proteinopathy and hippocampal sclerosis in relation to APOE ε4 haplotype status: A community-based cohort study. *Lancet Neurol.* **17**, 773–781 (2018). doi:10.1016/S1474-4422(18)30251-5 Medline
74. K. A. Josephs, J. L. Whitwell, S. D. Weigand, M. E. Murray, N. Tosakulwong, A. M. Liesinger, L. Petrucelli, M. L. Senjem, D. S. Knopman, B. F. Boeve, R. J. Ivnik, G. E. Smith, C. R. Jack Jr., J. E. Parisi, R. C. Petersen, D. W. Dickson, TDP-43 is a key player in the clinical features associated with Alzheimer's disease. *Acta Neuropathol.* **127**, 811–824 (2014). doi:10.1007/s00401-014-1269-z Medline
75. L. Van Helleputte, M. Kater, D. P. Cook, C. Eykens, E. Rossaert, W. Haeck, T. Jaspers, N. Geens, P. Vanden Berghe, C. Gysemans, C. Mathieu, W. Robberecht, P. Van Damme, G. Cavaletti, M. Jarpe, L. Van Den Bosch, Inhibition of histone deacetylase 6 (HDAC6) protects against vincristine-induced peripheral neuropathies and inhibits tumor growth. *Neurobiol. Dis.* **111**, 59–69 (2018). doi:10.1016/j.nbd.2017.11.011 Medline
76. M. L. Mauermann, M. S. Blumenreich, A. Dispenzieri, N. P. Staff, A case of peripheral nerve microvasculitis associated with multiple myeloma and bortezomib treatment. *Muscle Nerve* **46**, 964–970 (2012). doi:10.1002/mus.23493 Medline
77. A. Palanca, I. Casafont, M. T. Berciano, M. Lafarga, Reactive nucleolar and Cajal body responses to proteasome inhibition in sensory ganglion neurons. *Biochim. Biophys. Acta* **1842**, 848–859 (2014). doi:10.1016/j.bbadis.2013.11.016 Medline
78. D. G. Gibson, L. Young, R.-Y. Chuang, J. C. Venter, C. A. Hutchison 3rd, H. O. Smith, Enzymatic assembly of DNA molecules up to several hundred kilobases. *Nat. Methods* **6**, 343–345 (2009). doi:10.1038/nmeth.1318 Medline
79. H. B. Schmidt, A. Barreau, R. Rohatgi, Phase separation-deficient TDP43 remains functional in splicing. *Nat. Commun.* **10**, 4890 (2019). doi:10.1038/s41467-019-12740-2 Medline
80. F. J. Martinez, G. A. Pratt, E. L. Van Nostrand, R. Batra, S. C. Huelga, K. Kapeli, P. Freese, S. J. Chun, K. Ling, C. Gelboin-Burkhart, L. Fijany, H. C. Wang, J. K. Nussbacher, S. M. Broski, H. J. Kim, R. Lardelli, B. Sundararaman, J. P. Donohue, A. Javaherian, J. Lykke-Andersen, S. Finkbeiner, C. F. Bennett, M. Ares Jr., C. B. Burge, J. P. Taylor, F. Rigo, G. W. Yeo, Protein-RNA Networks Regulated by Normal and ALS-Associated Mutant HNRNPA2B1 in the Nervous System. *Neuron* **92**, 780–795 (2016). doi:10.1016/j.neuron.2016.09.050 Medline
81. M. F. Burkhardt, F. J. Martinez, S. Wright, C. Ramos, D. Volfson, M. Mason, J. Garnes, V. Dang, J. Lievers, U. Shoukat-Mumtaz, R. Martinez, H. Gai, R. Blake, E. Vaisberg, M. Grskovic, C. Johnson, S. Irion, J. Bright, B. Cooper, L. Nguyen, I. Griswold-Prenner, A. Javaherian, A cellular model for sporadic ALS using patient-derived induced pluripotent stem cells. *Mol. Cell. Neurosci.* **56**, 355–364 (2013). doi:10.1016/j.mcn.2013.07.007 Medline
82. S. M. Chambers, C. A. Fasano, E. P. Papapetrou, M. Tomishima, M. Sadelain, L. Studer, Highly efficient neural conversion of human ES and iPS cells by dual inhibition of SMAD signaling. *Nat. Biotechnol.* **27**, 275–280 (2009). doi:10.1038/nbt.1529 Medline
83. C. Vives-Bauza, C. Zhou, Y. Huang, M. Cui, R. L. A. de Vries, J. Kim, J. May, M. A. Tocilescu, W. Liu, H. S. Ko, J. Magrané, D. J. Moore, V. L. Dawson, R. Grailhe, T. M. Dawson, C. Li, K. Tieu, S. Przedborski, PINK1-dependent recruitment of Parkin to mitochondria in mitophagy. *Proc. Natl. Acad. Sci. U.S.A.* **107**, 378–383 (2010). doi:10.1073/pnas.0911187107 Medline
84. E. D. Schwoebel, T. H. Ho, M. S. Moore, The mechanism of inhibition of Ran-dependent nuclear transport by cellular ATP depletion. *J. Cell Biol.* **157**, 963–974 (2002). doi:10.1083/jcb.200111077 Medline
85. D. N. Mastronarde, Automated electron microscope tomography using robust prediction of specimen movements. *J. Struct. Biol.* **152**, 36–51 (2005). doi:10.1016/j.jsb.2005.07.007 Medline
86. S. Q. Zheng, E. Palovcak, J.-P. Armache, K. A. Verba, Y. Cheng, D. A. Agard, MotionCor2: Anisotropic correction of beam-induced motion for improved cryo-electron microscopy. *Nat. Methods* **14**, 331–332 (2017). doi:10.1038/nmeth.4193 Medline
87. D. N. Mastronarde, S. R. Held, Automated tilt series alignment and tomographic reconstruction in IMOD. *J. Struct. Biol.* **197**, 102–113 (2017). doi:10.1016/j.jsb.2016.07.011 Medline
88. Z. F. Yuan, C. Liu, H.-P. Wang, R.-X. Sun, Y. Fu, J.-F. Zhang, L.-H. Wang, H. Chi, Y. Li, L.-Y. Xiu, W.-P. Wang, S.-M. He, pParse: A method for accurate determination of monoisotopic peaks in high-resolution mass spectra. *Proteomics* **12**, 226–235 (2012). doi:10.1002/pmic.201100081 Medline
89. H. Chi, C. Liu, H. Yang, W.-F. Zeng, L. Wu, W.-J. Zhou, R.-M. Wang, X.-N. Niu, Y.-H. Ding, Y. Zhang, Z.-W. Wang, Z.-L. Chen, R.-X. Sun, T. Liu, G.-M. Tan, M.-Q. Dong, P. Xu, P.-H. Zhang, S.-M. He, Comprehensive identification of peptides in tandem mass spectra using an efficient open search engine. *Nat. Biotechnol.* **36**, 1059–1061 (2018). doi:10.1038/nbt.4236 Medline
90. C. Liu, C.-Q. Song, Z.-F. Yuan, Y. Fu, H. Chi, L.-H. Wang, S.-B. Fan, K. Zhang, W.-F. Zeng, S.-M. He, M.-Q. Dong, R.-X. Sun, pQuant improves quantitation by keeping out interfering signals and evaluating the accuracy of calculated ratios. *Anal. Chem.* **86**, 5286–5294 (2014). doi:10.1021/ac404246w Medline
91. K. Gasior, J. Newby, A. S. Gladfelter, Mathematical Modeling of liquid-liquid phase separation of TDP-43. (2020); https://doi.org/10.5281/zenodo.4287615.
92. J. Zhao, Mathematical Modeling of RNA-protein complexes under partial demixing conditions. (2017); https://doi.org/10.5281/zenodo.4299457.

ACKNOWLEDGMENTS

We thank Drs. E. Griffis and D. Bindels from the Nikon Imaging Center at UCSD for help on DIC and fluorescence microscopy. We thank Ms. Melissa McAlonis-Downes for preparing mouse DRG tissue samples. We acknowledge Y. Jones and V. Taupin in the UCSD School of Medicine Electronic Microscopy Facility for sample preparation and J. Santini from the UCSD School of Medicine Light Microscopy Core for assistance in fluorescence microscopy. We thank Sergey Suslov and Reika Watanabe for assistance with cryo-electron microscopy sample preparation and analysis. We thank Dr. T.J. Cohen for sharing TDP-43^{2KQ} variant and Dr. H.B. Broder for sharing the TDP-43 knockout HEK293T cell line. **Funding:** The authors thank the following funding support: D.W.C., NINDS R01-NS027036 and the NOMIS Foundation; H.Y., NIA F32-AG059358 and NINDS

K99-NS114162; K.G., NSF DMS-1816630; D.S., Damon Runyon Foundation DRG-2364-19; M.S.B., NIGMS T32-GM008666; J.R.Y., NIGMS P41-GM103533; J.M.N., the NSERC (RGPIN-2019-06435, RGPAS-2019-00014, DGECR-2019-00321), and NSF (DMS-171474, DMS-1816630); S.D.C., NINDS R01-NS027036; M.L., CIBERNED, CB06/05/0037; A.S.G., NIGMS R01-GM081506; E.V., The Pew Charitable Trust Scholars Program and NSF MRI DBI-1920374; UCSD microscopy core, NINDS P30-NS047101. The UC San Diego cryo-Electron Microscopy Facility is partially funded by a gift from the Agouron Institute.
Author contributions: H.Y., S.L., S.V.S. and D.W.C. designed most of the experiments. H.Y., S.L., S.V.S. performed most of the experiments. K.G., J.N. and A.S.G. designed and performed the mathematical modeling. D.S. and E.V. designed and performed the Cryo-ET. O.T. and M.L. designed and performed the EM and immunoEM in rat DRG neurons. D.T. helped in generating key materials. J.R.Y. supervised the proteomic experiments and analyses. H.Y., K.G. and D.W.C. wrote the original draft. A.S.G., E.V., N.J., M.L., S.D.C. and S.V.S. reviewed and edited the manuscript. **Competing interests:** A.S.G. is on the scientific advisory board of Dewpoint Therapeutics. The other authors declare no competing interests. **Data and materials availability:** All data are presented in the paper and/or the supplementary materials. Computer codes used in mathematical modeling are publicly available on Zenodo (Accession Numbers: 4287615 and 4299457) (*91*, *92*). Plasmids and cell lines generated by this research are available from Don W. Cleveland under a material agreement with the Ludwig Institute for Cancer Research Ltd. Requests should be submitted to dcleveland@health.ucsd.edu.

SUPPLEMENTARY MATERIALS

science.sciencemag.org/cgi/content/full/science.abb4309/DC1
Figs. S1 to S15
Tables S1 and S2
References
MDAR Reproducibility Checklist
Movies S1 to S4

8 March 2020; resubmitted 5 October 2020
Accepted 2 December 2020
Published online 17 December 2020
10.1126/science.abb4309

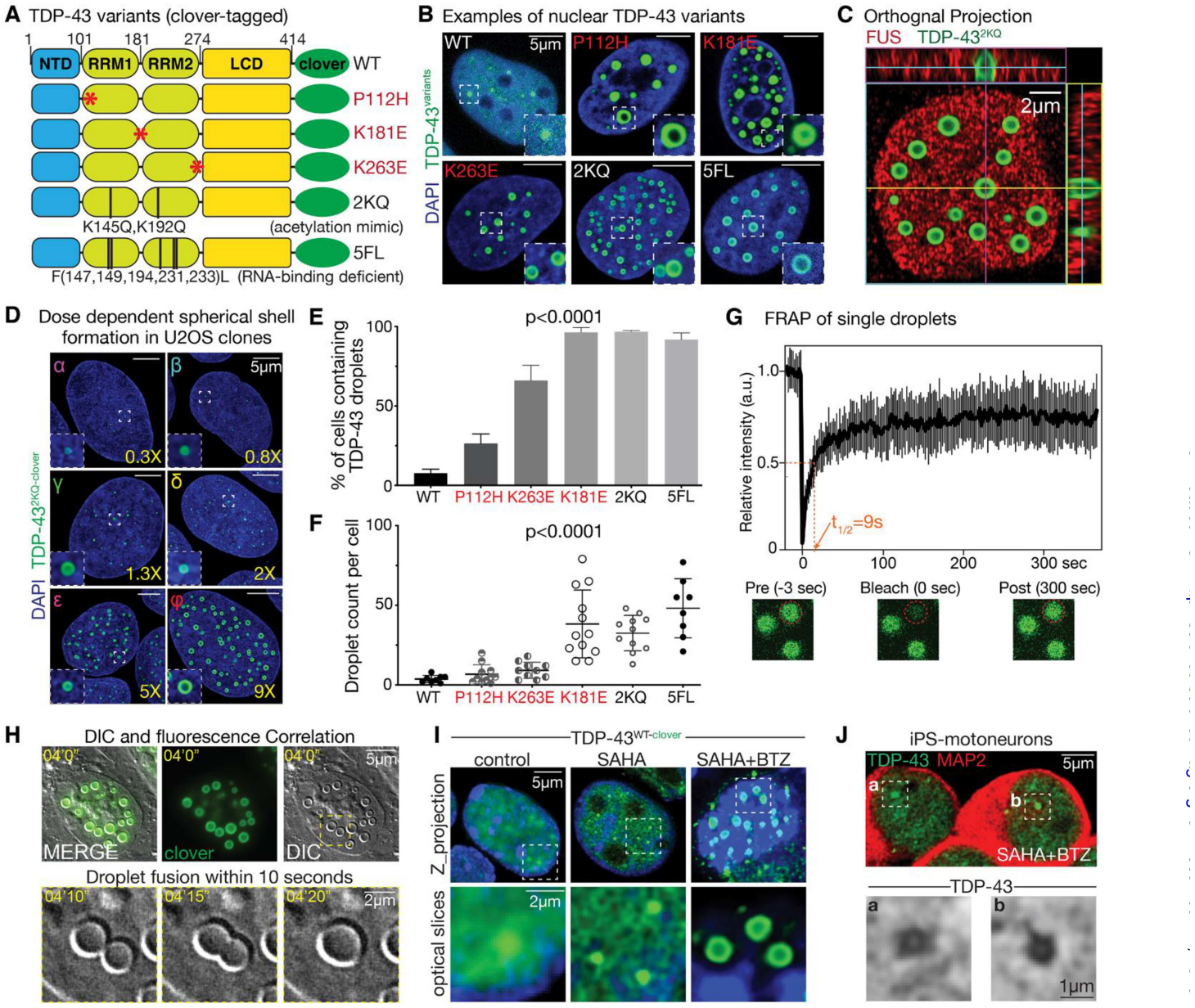

Fig. 1. RNA-binding deficient TDP-43 naturally de-mixes into intranuclear liquid spherical shells. (A) Schematic of TDP-43 wildtype and mutant proteins. All proteins were tagged at the carboxyl-terminus with the bright GFP variant, clover. (B) U2OS cells induced to express TDP-43 variants develop many more nuclear droplets than do cells expressing wildtype TDP-43. (*Dashed boxes*) Examples of nuclear droplets and magnified at the lower right corners. (C) Orthogonal projections demonstrate that TDP-43$^{2KQ\text{-clover}}$ droplets have nearly perfectly round spherical shells. (D) Spherical shell formation is dose dependent. (*Lower right*) TDP-43$^{2KQ\text{-clover}}$ expression level (relative to endogenous TDP-43) in each clone (determined as in fig. S1, C to F) is marked at the lower right of each image. (E and F) Quantified percentages of cells containing (E) TDP-43 droplets and (F) number of nuclear droplets per cell in U2OS cells expressing clover-tagged TDP-43 variants. (G) Liquid-like character of intranuclear TDP-43$^{2KQ\text{-clover}}$ spherical shells, demonstrated by rapid fluorescence recovery after photobleaching (FRAP). (H) Dynamic fusion of TDP-43$^{2KQ\text{-clover}}$ spherical shells visualized by live cell differential interference contrast (DIC) microscopy. Two spherical shells (1-2 μm) fuse into one (>2 μm) within 10 s. Inhibition of HDAC and proteasome activity synergize to enhance TDP-43 anisosome formation in neuron-like SHSY-5Y cells (I) and in iPSC-derived motor neurons (J).

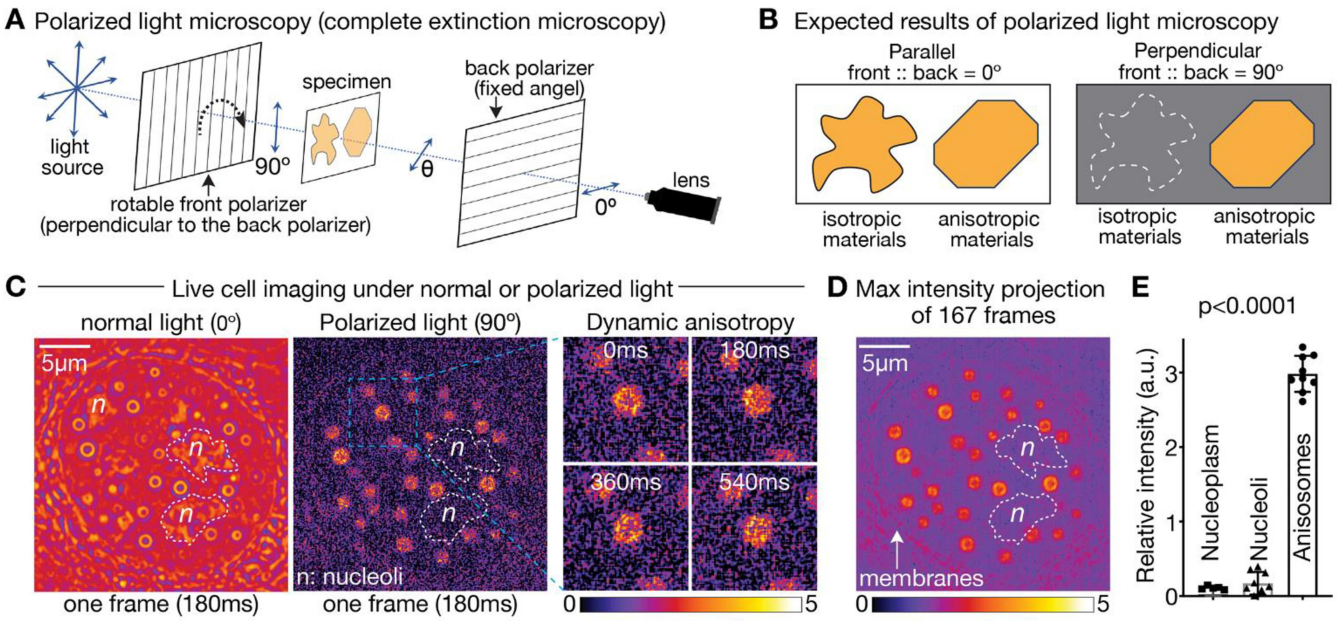

Fig. 2. TDP-43 intranuclear liquid spherical shells are anisotropic compartments of anisosomes. (A) Schematic of complete extinction microscopy. The light path contains two polarizers: the front polarizer can be adjusted from 0° to 90°, and the back polarizer has a fixed angle. Rotating the front polarizer result in a change of polarized light. (B) Only anisotropic materials can be distinguished by complete extinction microscopy because the birefringent property of the anisotropic material allows some light to pass the back polarizer. (C) The same nucleus containing TDP-43 liquid spherical shells is imaged under normal or polarized light sources (images are pseudocolored to display intensity of light). Phase-separated nucleoli (marked by "*n*") cannot be detected when the polarized light is perpendicular to the filter. (*Dashed box*) Magnified view of the dynamic anisotropic sub-domains. (D) Maximum intensity projection of images in (C) (167 frames in 30 s of live imaging under complete extinction conditions). Arrow points to membranes, a known anisotropic structure – the lipid bilayer. (E) Quantification of signal intensity of nucleoplasm, nucleoli, and anisosomes.

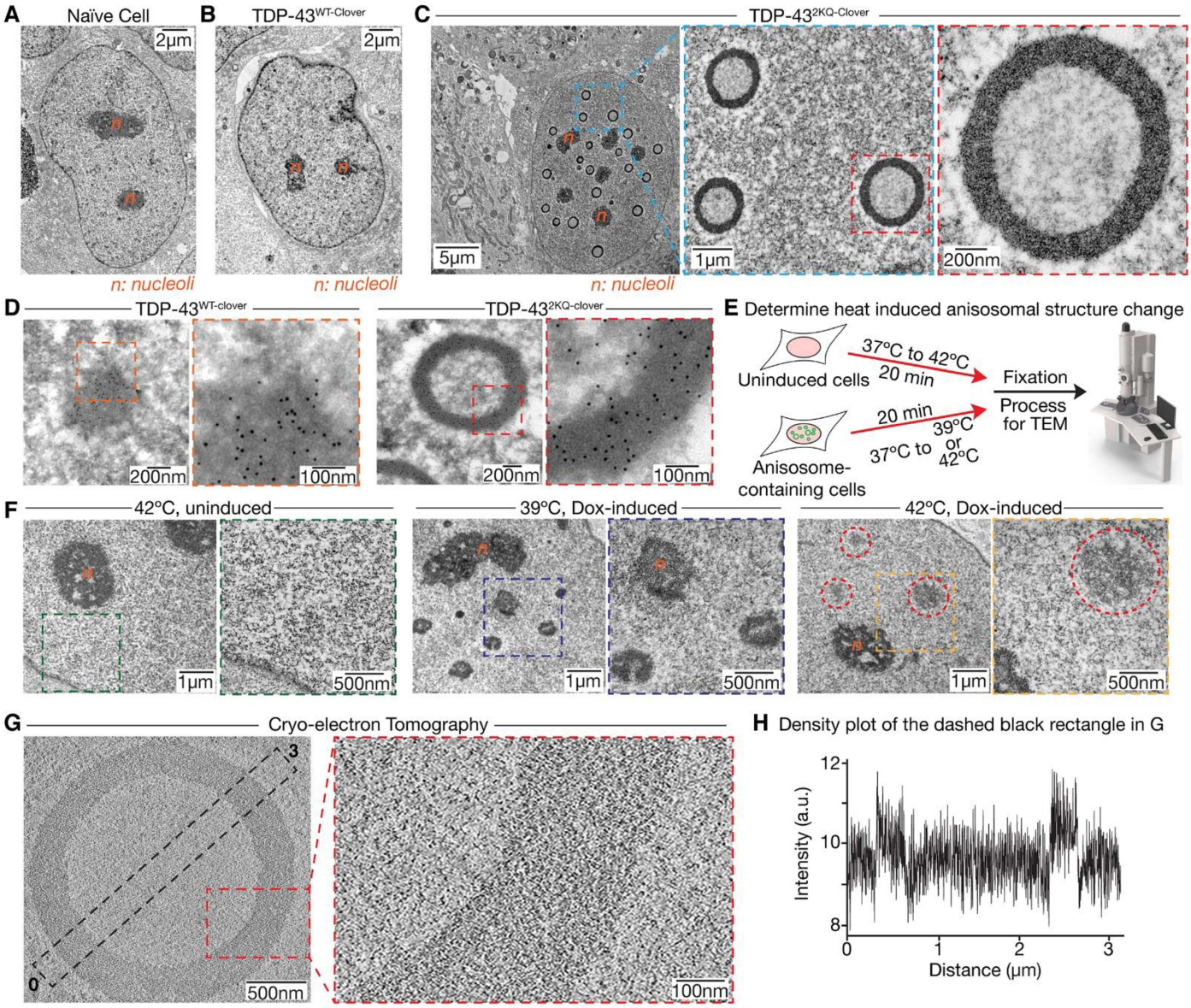

Fig. 3. TDP-43 anisosomes are membraneless compartments with densely packed shells visualized by transmission electron microscopy (TEM) and cryo-electron tomography (CryoET). TEM examples of nuclei from (A) a naïve U2OS cell, (B) a U2OS cell expressing TDP-43$^{WT\text{-}clover}$, and (C) a U2OS cell expressing TDP-43$^{2KQ\text{-}clover}$ (see additional examples in fig. S3). (D) Immunogold labeling with a GFP antibody of (*left*) a TDP-43$^{WT\text{-}clover}$ droplet or (*right*) a TDP-43$^{2KQ\text{-}clover}$ anisosome. (*Dashed boxes*) Enlarged views of the distribution of gold particles (see fig. S4 for additional examples). (E) Schematic of 20-min temperature shift and determination of the structural changes with TEM. (F) A temperature shift-induced structural change visualized by TEM. (*Dashed boxes*) Magnified views of each condition. At 42°C, no irregular structure was observed in the nucleoplasm without the induction of anisosomes. At 39°C, anisosomes become irregular shape, while at 42°C, irregular shape and less electron dense. (Dashed r*ed circles*) Irregular electron dense compartments. (G) Cryo-electron tomography of an anisosome and (H) density plot of the area enclosed in the dashed black rectangle.

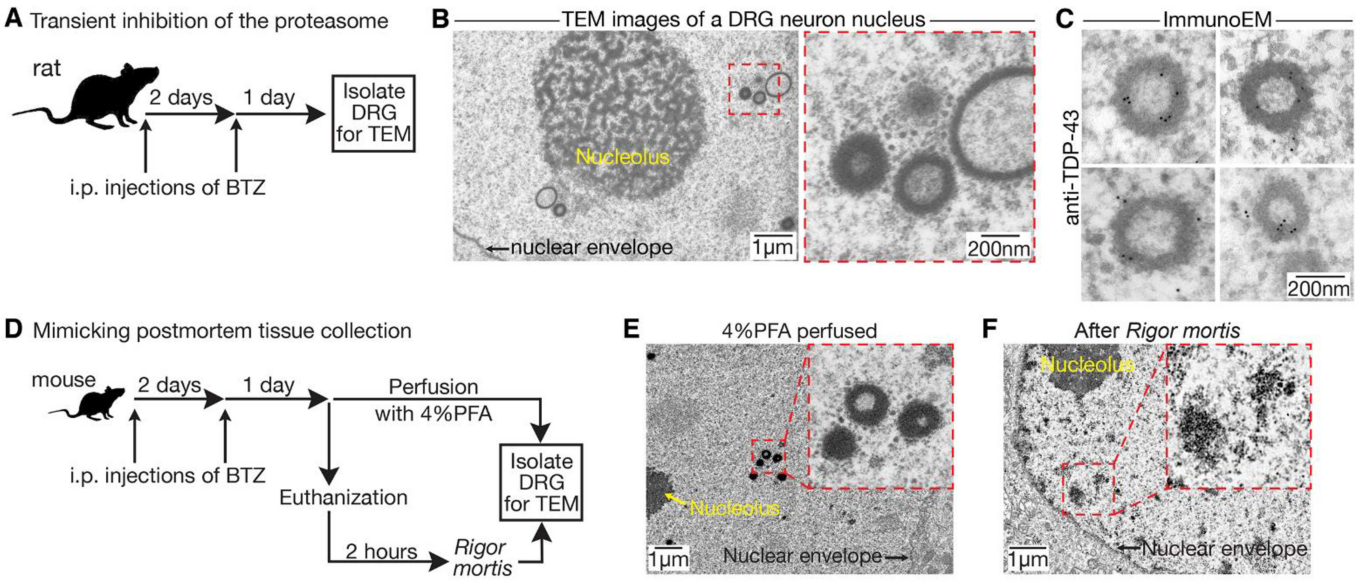

Fig. 4. Proteolytic stress in neurons of the adult nervous system induces TDP-43-containing anisosomes, which convert into aggregates as ATP levels fall. (A) Schematic of experimental steps for inducing transient proteolytic stress in Sprague Dawley rats by intravenous (i.v.) administration of the proteasome inhibitor bortezomib (BTZ). (B) TEM images of intranuclear spherical shells found in nuclei of DRG sensory neurons from mice treated as in (A). (*Dashed red square*) area magnified at right. (C) Immunogold labeling for endogenous TDP-43 in bortezomib-induced spherical shells. (D) Schematic of induction of TDP-43-containing spherical shells in mouse DRG neurons by partial proteasome inhibition and then examined after immediate or delayed tissue collection. Images of DRGs collected (E) immediately after perfusion or (F) after a 2-hour postmortem delay during which ATP levels falls sufficiently to initiate rigor mortis. Anisosomes seen in freshly fixed samples convert to amorphous dense intranuclear structures after postmortem delay.

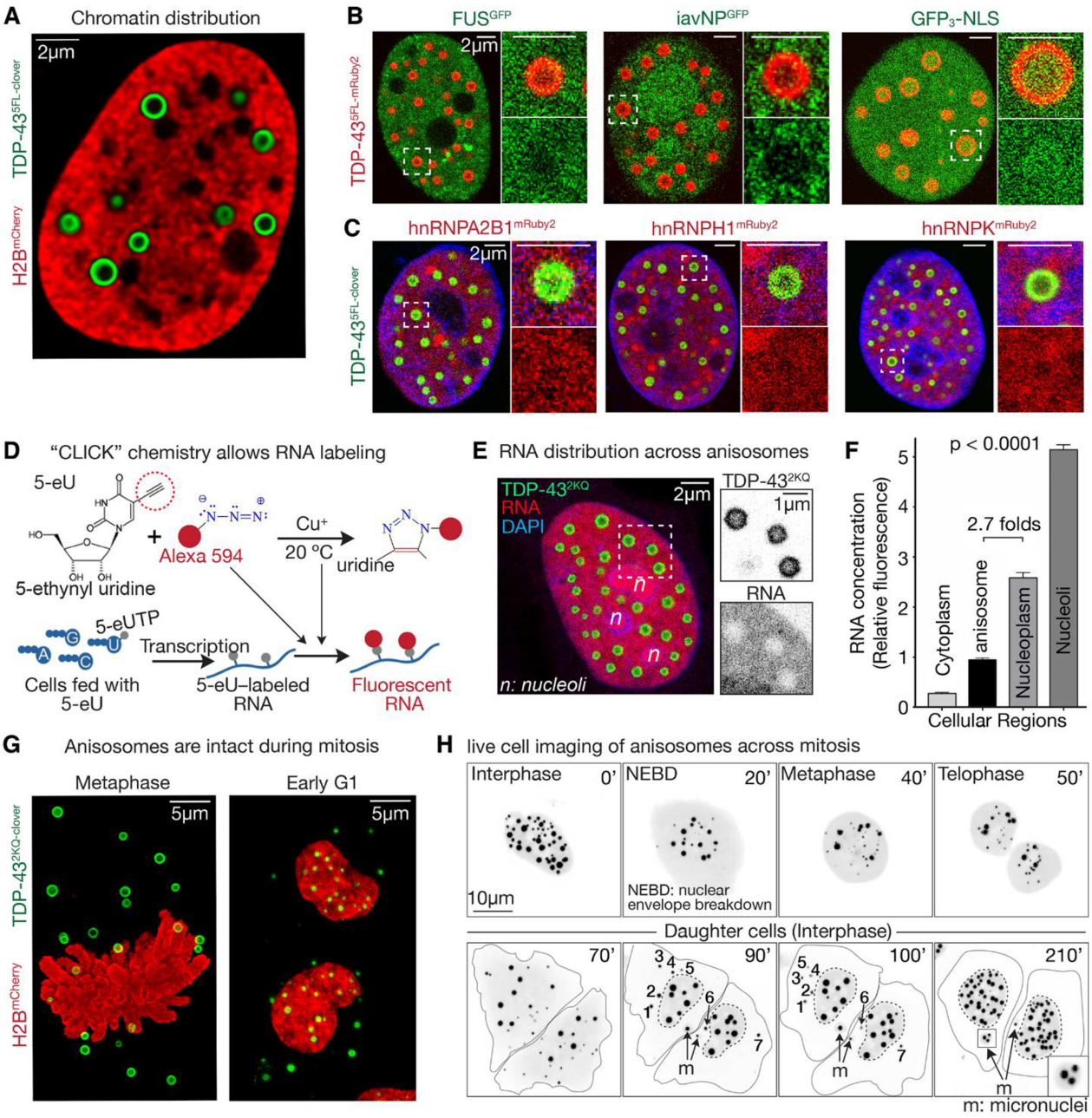

Fig. 5. TDP-43 anisosomes, intact during mitosis, are selective barriers for RNA and some nuclear proteins. (A) A U2OS nucleus stably expressing H2B^{mCherry}, a fluorescent histone marker and TDP-43$^{5FL\text{-}clover}$. (B and C) Fluorescence imaging of nuclear RNA-binding proteins (B) hnRNPA2B1, hnRNPH1 and hnRNPK (each carboxy-terminally tagged with mRuby2) or (C) EGFP-labeled FUS, iavNP or EGFP alone. (D) Schematic for fluorescent labeling of cellular RNA with "CLICK" chemistry. (E) Imaging of anisosomes of TDP-43^{2KQ} and nuclear RNA (labeled as in (D)). (F) Quantification of fluorescence intensity of the RNA in (E). (G) Imaging of TDP-43 anisosomes in mitotic and post-mitotic cytoplasm and post-mitotic reassembly within daughter nuclei. (H) An imaging series of TDP-43$^{2KQ\text{-}clover}$ anisosomes during mitosis and early interphase. (Solid lines) The cell plasma membrane; (dashed lines) outline of the nuclear envelope. The numbers 1-7 denote specific cytoplasmic TDP-43$^{2KQ\text{-}clover}$ droplets, each of which becomes smaller within 10 min. (*m*) Anisosomes reforming within micronuclei produced by mitotic chromosome segregation errors.

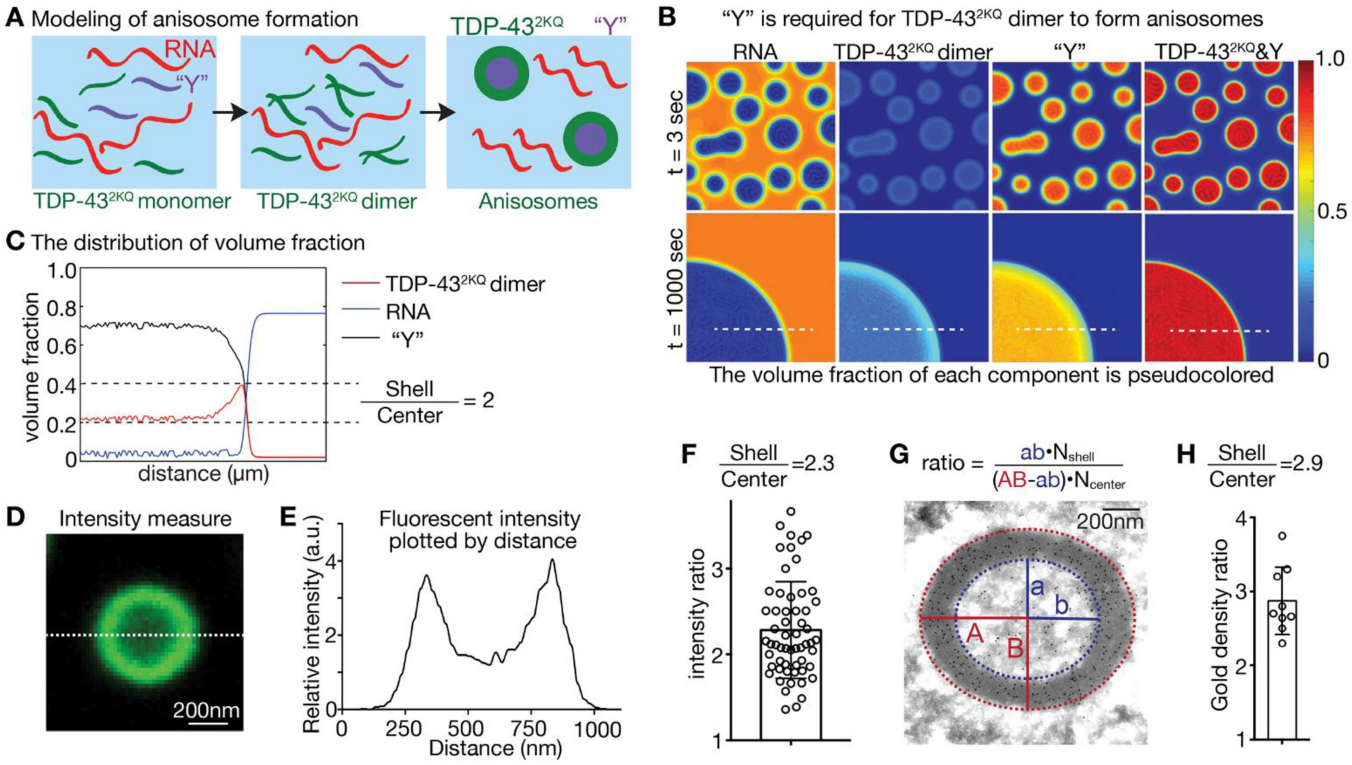

Fig. 6. **Mathematical modeling predicts that a third component is required for anisosomal formation and maintenance.** (A) Schematic of modeling of anisosome formation by TDP-43^{2KQ} mutant in a simple mixture of TDP-43, RNA, and a proposed Y molecule that has high affinity for itself, low affinity for TDP-43, and no RNA binding. (B) A snapshot from the model in (A) of de-mixing at 3 and 1000 s after starting from a uniform solution. (C) The volume fraction of each species from modeling in (A and B) at a 1000 s time point. The ratio of volume fraction between the shell and the center of the anisosome for TDP-43^{2KQ} is about 2. Clover fluorescence intensity across TDP-43^{2KQ} anisosomes. (D) An optical slice of an anisosome with (E) intensity of the dashed line in (D). (F) The quantified ratio between the shell and the center, with a mean of 2.28 ± 0.56 (SD). (G) Measurement of the ratio of gold particle density in immunogold-labeling of TDP-43$^{2KQ\text{-clover}}$ in an anisosome and (H) quantification of the ratio of gold particle density between the shell and the center.

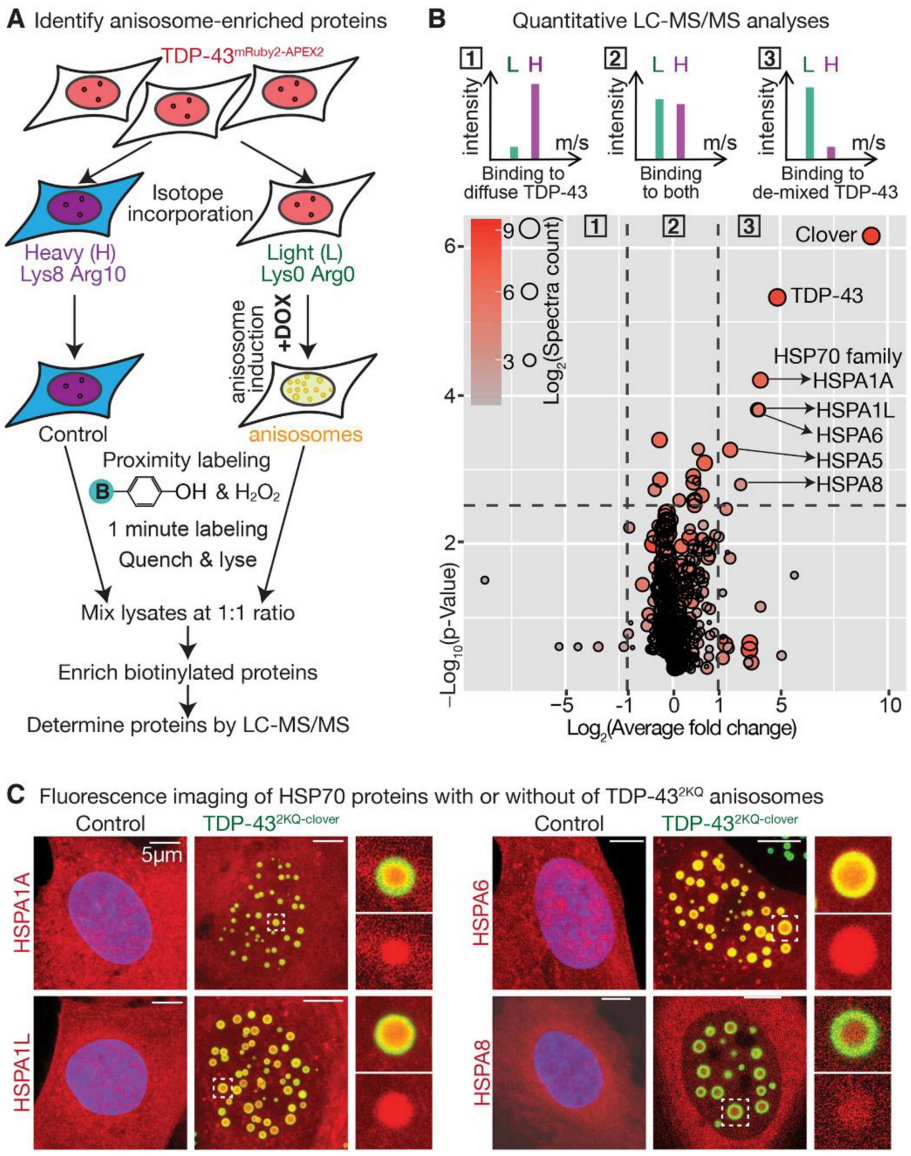

Fig. 7. **The HSP70 family of molecular chaperones are specifically enriched in cores of TDP-43 anisosomes.** (**A**) Schematic of APEX2-mediated proximity labeling followed by quantitative proteomic analyses (see also fig. S10). (**B**) Quantitative proteomic analyses identify HSP70 family proteins to be enriched in the cores of de-mixed TDP-43 anisosomes. Y axis is p-value at $\log_{10}$ scale; X axis is fold enrichment on $\log_2$ scale. The size and color of each spot correspond to the total spectral counts of LC/MS-MS reads on $\log_2$ scale. (**C**) Maximum intensity projections of immunofluorescence images of U2OS nuclei expressing (*green*) TDP-43$^{2KQ\text{-clover}}$ anisosomes and (*red*) HSP70 family proteins tagged by mRuby2. (*White boxes*) Boxed areas that are magnified at right.

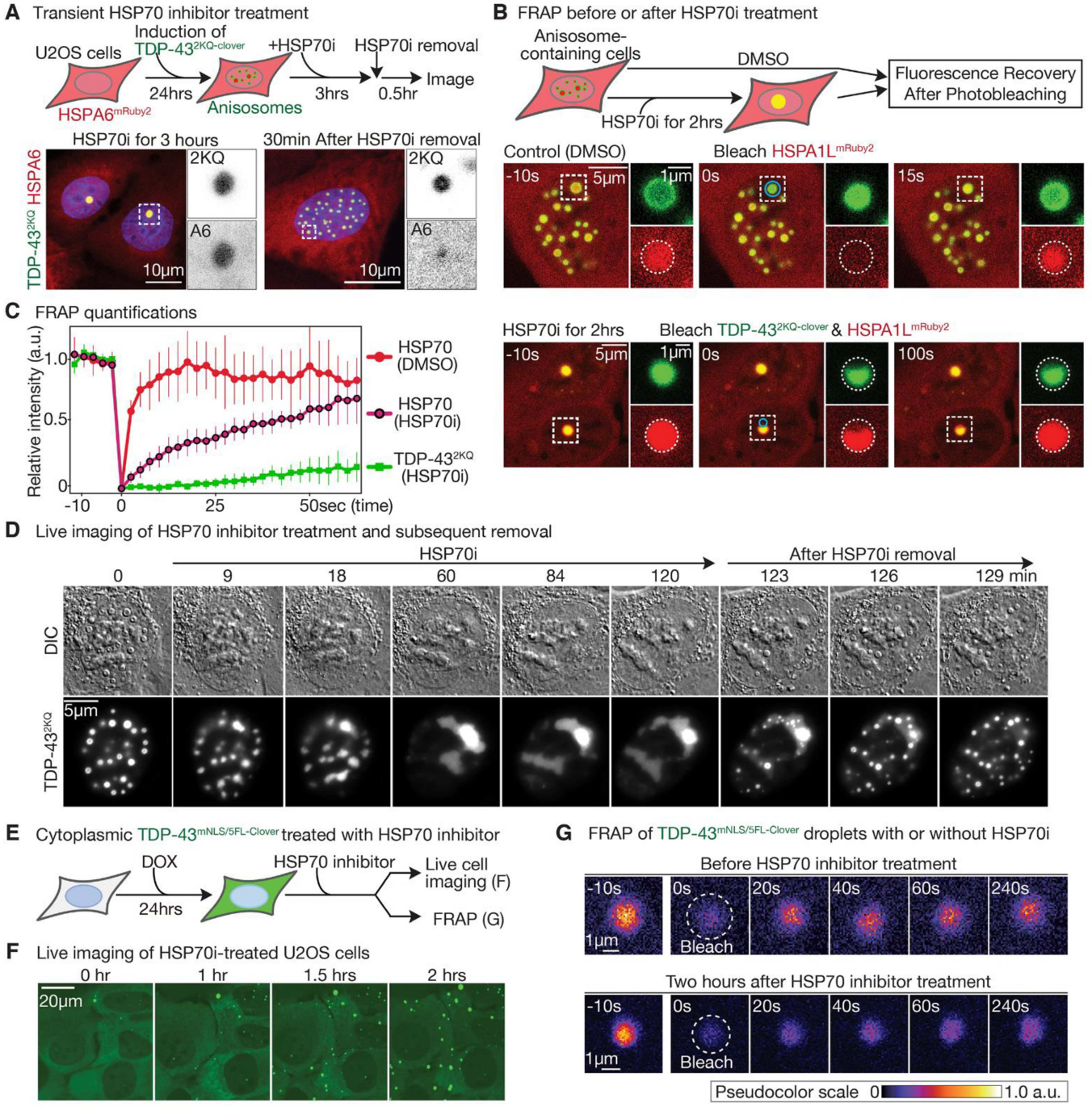

Fig. 8. The ATP-dependent chaperone activity of the HSP70 family chaperones regulate anisosomal structure and liquidity of both shells and cores. (A) Imaging of anisosomes formed after transient induction of TDP-43$^{2KQ\text{-}clover}$ in cells stably expressing HSPA6^{mRuby2} after (*left*) addition of an HSP70 ATPase inhibitor (VER155008) and (*right*) after a subsequent 0.5 hour wash out of the inhibitor. (B) (*Top*) Schematic of FRAP of anisosomes formed in cells in (A) in the absence of or after addition the HSP70 inhibitor. (*Middle*) FRAP of HSPA1L^{mRuby2} in TDP-43$^{2KQ\text{-}clover}$ anisosomes. (*Bottom*) FRAP of a portion of a TDP-43$^{2KQ\text{-}clover}$ and HSPA1L^{mRuby2}-containing intranuclear droplet in cells treated with the HSP70 inhibitor. (C) Kinetics of the FRAP experiments in (B). HSP70^{mRuby2} quickly recovers after bleaching (the red curve, $\tau < 2$ s), but is much less dynamic after HSP70 inhibitor treatment (the purple curve, τ is between 40 and 42.5 s). In the HSP70 inhibitor, only a small proportion of TDP-43$^{2KQ\text{-}clover}$ recovers, which recovers slowly. (D) Live DIC and fluorescence imaging of TDP-43$^{2KQ\text{-}clover}$ in anisosomes after addition and wash out of the HSP70 inhibitor. (E) Schematic of addition and imaging of diffuse cytoplasmic TDP-43$^{NLSm/5FL\text{-}clover}$ after addition of the HSP70 inhibitor. (F) Live fluorescence imaging of TDP-43$^{NLSm/5FL\text{-}clover}$ assembly into cytoplasmic droplets upon addition of the HSP70 inhibitor. (G) FRAP of cytoplasmic droplets from (F).

HSP70 chaperones RNA-free TDP-43 into anisotropic intranuclear liquid spherical shells

Haiyang Yu, Shan Lu, Kelsey Gasior, Digvijay Singh, Sonia Vazquez-Sanchez, Olga Tapia, Divek Toprani, Melinda S. Beccari, John R. Yates III, Sandrine Da Cruz, Jay M. Newby, Miguel Lafarga, Amy S. Gladfelter, Elizabeth Villa and Don W. Cleveland

published online December 17, 2020

Science (print ISSN 0036-8075; online ISSN 1095-9203) is published by the American Association for the Advancement of Science, 1200 New York Avenue NW, Washington, DC 20005. The title *Science* is a registered trademark of AAAS.